

# Black hole–neutron star binaries with high spins and large mass asymmetries: I. Properties of quasi-equilibrium sequences

Konrad Topolski <sup>1</sup>, Samuel D. Tootle <sup>2,1</sup> and Luciano Rezzolla <sup>1,3,4</sup>

<sup>1</sup>*Institut für Theoretische Physik, Goethe Universität, Max-von-Laue-Str. 1, 60438 Frankfurt am Main, Germany*

<sup>2</sup>*Department of Physics, University of Idaho, Moscow, ID 83843, USA*

<sup>3</sup>*Frankfurt Institute for Advanced Studies, Ruth-Moufang-Str. 1, 60438 Frankfurt, Germany*

<sup>4</sup>*School of Mathematics, Trinity College, Dublin 2, Ireland*

(Dated: September 12, 2024)

Black hole – neutron star (BHNS) mergers are a promising target of current gravitational-wave (GW) and electromagnetic (EM) searches, being the putative origin of ultra-relativistic jets, gamma-ray emission, and r-process nucleosynthesis. However, the possibility of any EM emission accompanying a GW detection crucially depends on the amount of baryonic mass left after the coalescence, i.e., whether the neutron star (NS) undergoes a “tidal disruption” or “plunges” into the black hole (BH) while remaining essentially intact. As the first of a series of two papers, we here report the most systematic investigation to date of quasi-equilibrium sequences of initial data across a range of stellar compactnesses  $\mathcal{C}$ , mass ratios  $q$ , BH spins  $\chi_{\text{BH}}$ , and equations of state satisfying all present observational constraints. Using an improved version of the elliptic initial-data solver FUKA, we have computed more than 1000 individual configurations and estimated the onset of mass-shedding or the crossing of the innermost stable circular orbit in terms of the corresponding characteristic orbital angular velocities  $\Omega_{\text{MS}}$  and  $\Omega_{\text{ISCO}}$  as a function of  $\mathcal{C}$ ,  $q$ , and  $\chi_{\text{BH}}$ . To the best of our knowledge, this is the first time that the dependence of these frequencies on the BH spin is investigated. In turn, by setting  $\Omega_{\text{MS}} = \Omega_{\text{ISCO}}$ , it is possible to determine the separatrix between the “tidal disruption” or “plunge” scenarios as a function of the fundamental parameters of these systems, namely,  $q$ ,  $\mathcal{C}$ , and  $\chi_{\text{BH}}$ . Finally, we present a novel analysis of quantities related to the tidal forces in the initial data and discuss their dependence on spin and separation.

## I. INTRODUCTION

There is now convincing evidence obtained via gravitational-wave (GW) detections that black hole – neutron star (BHNS) binary systems exist in nature and undergo merger events [1]. More so, GW events continue to provide evidence for binaries in nature to include BHs in the range of  $3 - 5 M_{\odot}$  [2], a “mass gap” that is clearly being filled by continued GW detections. As in the case of neutron star–neutron star (NSNS) binary systems, such as GW170817 [3], a rich set of electromagnetic (EM) counterparts are expected from a BHNS merger [4].

In light of the difficulties of differentiating between a black hole – black hole (BBH) and a BHNS system based on the GW signal alone, binaries in which the neutron star (NS) undergoes a tidal disruption are of particular interest. The process of tidal disruption in numerical simulations has been shown to leave behind a massive torus [5–13], whose nontrivial interactions with the magnetic field [14] and the presence of neutrino radiation [15] potentially drive a variety of discernible EM signals [16] on a wide range of timescales, ranging from hundreds of milliseconds to weeks (see, for example [17]). Understanding the conditions under which a tidal disruption occurs, quantifying its effects on the GW signal and its feedback on the equation of state (EOS) [18–20], predicting the mass of the remnant black hole (BH) and its spin [21–23], as well as the mass of the formed accretion disc and dynamical ejecta [24–28], have all been studied in numerous papers in the context of general-relativistic magnetohydrodynamical (GRMHD) simulations. Furthermore, a number of investigations have looked into fully three-dimensional evolution of the post-merger BH and torus configuration on timescales of several hundred milliseconds [29–32] to several

seconds [33–35], predicting substantial Poynting fluxes owing to the Blandford-Znajek energy extraction mechanism [36], coincident with a collimated outflow with appreciable Lorentz factors (albeit limited due to numerical difficulties associated with the conservative-to-primitive recovery and insufficiently low atmosphere levels) and high magnetization [34] far away from the jet launching site (see [37] for a summary of the most recent developments with regards to seconds-long evolutions in the post-merger phase).

This work is the first in a series of two papers in which we investigate the properties of BHNS systems under a variety of gravitational and microphysical conditions. This paper (paper I), in particular, reports the study of quasi-equilibrium (QE) sequences of BHNS binaries obtained as solutions to the constraint equations on an initial hypersurface under an assumption of time-symmetry and orbital circularity. Studies of this type have a long history beginning with the seminal work by Taniguchi and collaborators [38–40], who constructed QE sequences using the BH excision approach, for a simple polytropic EOS with the adiabatic index  $\Gamma = 2$  [41], and provided estimates for the orbital angular velocity at tidal disruption and innermost stable circular orbit. At the same time, Grandclement [42] pursued the same goal and obtained similar results for the binding energy, with some differences in the quantity predicting the tidal disruption, while Kyutoku and collaborators [43] investigated sequences where the BH is represented by a puncture and obtained similar results for the mass-shedding diagnostics, but noted deviations in the binding energy when compared to the excision approach.

The extension of these initial studies to more realistic configurations which include both a spinning primary (i.e., the BH) and realistic EOSs has been relatively limited and aimed mostly at showcasing the abilities and convergence properties

of new and advanced initial-data solvers [44–47]. To bridge this gap, we here report the most systematic investigation to date of QE sequences of initial data across a range of stellar compactnesses  $\mathcal{C} := M/R$ , with  $M$  and  $R$  being the stellar gravitational mass and radius, respectively; binary mass ratios  $q := M_{\text{NS}}/M_{\text{BH}}$ , with  $M_{\text{BH}}$  and  $M_{\text{NS}}$  being the BH and NS gravitational masses, respectively; (dimensionless) BH spins  $\chi_{\text{BH}}$ , and EOSs satisfying all present observational constraints. For simplicity, and to ensure a reasonable size of the space of parameters, we will not investigate QE sequences with spinning NSs and set  $\chi_{\text{NS}} = 0$  accordingly. A follow-up study will also discuss the influence of the secondary spin.

This paper I has a number of different purposes. First, it highlights the capabilities of an improved version of the publicly available Frankfurt-University-Kadath (FUKA) [47, 48] codes, which has been shown to yield accurate initial data under a number of conditions in the binary [49, 50] and that is becoming a reference choice in many numerical-relativity groups [51–56]. Second, it offers a comprehensive view of the dependence of the onset of mass-shedding or the crossing of the innermost stable circular orbit in terms of the corresponding characteristic orbital angular velocities  $\Omega_{\text{MS}}$  and  $\Omega_{\text{ISCO}}$  as a function of  $\mathcal{C}$ ,  $q$ , and  $\chi_{\text{BH}}$ . In this way, and by setting  $\Omega_{\text{MS}} = \Omega_{\text{ISCO}}$ , it is possible to determine the separatrix between the “tidal disruption” and “plunge” scenarios as a function of  $q$ ,  $\mathcal{C}$ , and  $\chi_{\text{BH}}$ . Finally, the paper guides the set of initial conditions for the dynamical evolution of a large number of BHNS systems that will be presented in paper II [57].

The paper is organized as follows. In Sec. II, we briefly summarise the elliptic equations which are solved to obtain the QE sequences and define the key diagnostic quantities that allow us to judge the quality of the solutions. In Sec. III, we shortly describe the numerical setup in the FUKA code, outline the covered space of binary parameters, and the methods used to extract the relevant information from a sequence. Therein, a novel analysis of tidal forces on an initial data hypersurface is also presented. The results for irrotational sequences for three cold EOSs are presented in Sec. IV, preceded by a comparison of  $\Gamma = 2$  polytrope predictions by [40]. The section concludes with a study of QE sequences with a spinning BH and includes new results on the spin dependence of the mass-shedding diagnostic and the location of an effective innermost stable circular orbit. Also discussed is the nontrivial dependence of binding energy values on BH spin for realistic mass-ratio sequences. We summarise the main findings of our work in Sec. V and suggest possible improvements and avenues that could be explored. Throughout the paper, we use the geometrical units  $G = c = 1$ , where  $G$  and  $c$  are the gravitational constant and the speed of light, respectively. Greek (Latin) indices run from 0 (1) to 3.

## II. MATHEMATICAL SETUP: THE XCTS SYSTEM IN QUASI-EQUILIBRIUM

The foundation of this work is the use of the publicly available FUKA initial data code originally described in [58] with significant advancements included in the second version of

FUKA [48], which provides a highly robust solver infrastructure to compute incredibly challenging initial data sequences such as those which will be discussed in Sec. IV, in addition to BBH and BNS configurations. Here we will briefly describe the system of equations solved by FUKA followed by an overview of the numerical implementation in Sec. III.

To solve the initial value problem on a spacelike hypersurface in GR, FUKA computes solutions to the widely used eXtended Conformal Thin Sandwich (XCTS) formalism [59, 60], which is customarily applied for generating QE configurations, i.e., quasi-circular orbits and approximately time-symmetric. For a spacetime to be in *quasi-equilibrium*, the existence of a helical symmetry vector  $\xi^\mu := \partial_t^\mu + \Omega \partial_\varphi^\mu$  is assumed, where the (inertial) coordinate time vector  $\partial_t^\mu := \alpha n^\mu + \beta^\mu$  is built from the lapse function  $\alpha$ , the normal vector to the hypersurface  $n^\mu$ , and the shift vector  $\beta^\mu$ . Similarly, the azimuthal component in  $\xi$  is expressed in terms of the orbital angular velocity of the binary  $\Omega$ , with  $\partial_\varphi$  the vector field generating the rotational symmetry. Should such a vector field  $\xi$  exist, all tensor fields  $\mathcal{T}$  in the spacetime would be invariant under the symmetry group it generates, which is expressed as the vanishing of Lie derivatives  $\mathcal{L}_\xi \mathcal{T} = 0$ . The existence of a global helical symmetry implies in particular that  $\xi$  is a Killing vector field. We will henceforth often refer to  $\xi$  as a Killing vector, understanding that it can represent a more general and deeper symmetry.

In this work we consider only conformally flat initial data where the purely spatial metric,  $\gamma_{ij}$ , is approximated as  $\gamma_{ij} = \psi^4 \tilde{\gamma}_{ij}$ . This decomposition drastically simplifies the system of equations as  $\tilde{\gamma}_{ij}$  is a fixed conformal metric with a flat connection ( $\text{Riem}[\tilde{\gamma}] = 0$ , e.g.,  $\delta_{ij}$ ) and  $\psi$  is the conformal factor that simply rescales  $\tilde{\gamma}_{ij}$  locally. The extrinsic curvature tensor  $K_{ij}$  is correspondingly decomposed into the conformal trace-free part  $\hat{A}_{ij}$  and the trace  $K := \gamma^{ij} K_{ij}$  as

$$K_{ij} = \psi^{-2} \hat{A}_{ij} + \frac{1}{3} K \gamma_{ij}. \quad (1)$$

In this way, the condition of QE simplifies the system of equations considerably and is imposed by demanding that the derivatives of the trace of the extrinsic curvature and the conformal metric vanish, i.e.,  $\mathcal{L}_\xi K = 0 = \mathcal{L}_\xi \tilde{\gamma}_{ij}$ . Such a specification, combined with enforcing the maximal slicing condition,  $K = 0$ , completes the choice of the *free data* of the XCTS scheme.

The elliptic equations of the initial-data system that are implemented in FUKA provide a solution for the conformal factor  $\psi$ , the lapse  $\alpha$ , the inertial shift vector  $\beta^i$ , the extrinsic curvature tensor  $\hat{A}_{ij}$ , the corotating fluid velocity  $V^i$  and the logarithm of the specific enthalpy  $H := \ln h$ . The set of constraint

equations  $\{\mathcal{H}, \mathcal{C}_{\alpha\psi}, \mathcal{M}^i, \mathcal{C}_{v.p.}\}$  to be computed simplifies to<sup>1</sup>

$$\mathcal{H} := \tilde{D}^i \tilde{D}_i \psi + \frac{1}{8} \psi^{-7} \hat{A}^{ij} \hat{A}_{ij} + 2\pi \psi^5 E, \quad (2)$$

$$\mathcal{C}_{\alpha\psi} := \tilde{D}^i \tilde{D}_i (\alpha\psi) - \frac{7}{8} \alpha \psi^{-7} \hat{A}^{ij} \hat{A}_{ij} - 2\pi \alpha \psi^5 (E + 2S), \quad (3)$$

$$\mathcal{M}^i := \tilde{D}^j \tilde{D}_j \beta^i + \frac{1}{3} \tilde{D}^i \tilde{D}_j \beta^j - 2\hat{A}^{ij} \tilde{D}_j (\alpha\psi^{-6}) - 16\pi \alpha \psi^4 p^i, \quad (4)$$

$$\mathcal{C}_{v.p.} := \psi^6 W V^i \tilde{D}_i H + \frac{dH}{d \ln \rho} \tilde{D}_i (\psi^6 W V^i), \quad (5)$$

where the matter source terms  $(E, S, p^i)$  are the same as in [47] and read

$$E := \rho h W^2 - p, \quad (6)$$

$$S := 3p + (E + p)U^2, \quad (7)$$

$$p^i := \rho h W^2 U^i, \quad (8)$$

and

$$\hat{A}_{ij} := \frac{\psi^6}{2\alpha} (\tilde{D}^i \beta^j + \tilde{D}^j \beta^i - \frac{2}{3} \tilde{\gamma}^{ij} \tilde{D}_k \beta^k). \quad (9)$$

The relativistic specific enthalpy is  $h := 1 + \epsilon + p/\rho$  with pressure  $p$ , density  $\rho$  and specific internal energy  $\epsilon$ . In the above,  $U^i$  is the spatial projection of the four-velocity of the fluid,  $W := (1 - U^2)^{-1/2}$  is the associated Lorentz factor, and  $\tilde{D}^i$  denotes the covariant derivative compatible with the conformal metric  $\tilde{\gamma}$ . We have also defined the spatial corotating fluid velocity as  $V^i = \alpha U^i - \xi^i$ . Equation (5) determines the velocity potential (v.p.) and derives from the continuity equation, whereas  $\mathcal{C}_{\alpha\psi}$  is obtained directly from the dynamical evolution equation for the trace of the extrinsic curvature by setting the right-hand side of  $\mathcal{L}_\xi K$  and  $K$  itself to zero. FUKA solves the elliptic equations (2)–(5) to a desired precision and after adequate boundary conditions are imposed (see [47] for more details). Additionally, the approximate first integral of the relativistic Euler equation is imposed onto the NS matter

$$\log(h\alpha W^{-1} + \tilde{D}_i \Phi V^i) = C, \quad (10)$$

where the constant  $C$  is fixed depending on the value of the specific enthalpy  $h$  at the centre of the star. Finally, we must provide an EOS to close the system of equations. FUKA includes an EOS module that supports the use of (piecewise-)polytropic EOSs as well as 1D tabulated EOSs for realistic models which is yet another critical component that has enabled the novel exploration of this work.

The assumed stationarity of the solution can be validated by inspecting the violation of  $\xi$  to represent an asymptotically

timelike Killing vector. More specifically, we compute the *virial error*, defined as

$$\delta M := 1 - \frac{M_K}{M_{\text{ADM}}}, \quad (11)$$

where  $M_{\text{ADM}}$  and  $M_K$  are the ADM and Komar masses, respectively. Under the assumption of conformal flatness these masses are defined as [47]

$$M_{\text{ADM}} := -\frac{1}{2\pi} \int_{S_\infty} D_i \psi s^i d^2 \sigma, \quad (12)$$

$$M_K := \frac{1}{4\pi} \int_{S_\infty} D_i \alpha s^i d^2 \sigma, \quad (13)$$

where  $s^i$  is the spatial unit vector normal to the sphere of integration. We note that FUKA is well suited for computing the virial error as the physical space is decomposed in a multi-grid scheme with the outer spherical domain utilizing compactified spatial coordinates such that the outer spherical boundary,  $S_\infty$ , is mapped to spatial infinity rather than an arbitrary large number (see [61] for details).

As pointed out in Ref. [62], there exists a tension between the QE assumption for the fluid and the choice  $K = 0$  in the XCTS system of equations. This tension follows from deriving the continuity equation (cf., Eqs. (50) and (53) in [63]), where, among others, the term  $\mathcal{L}_\xi \ln \psi$  is set to zero<sup>2</sup>, which is not strictly enforced as part of the constraint equations despite it also being necessary for “true” QE. Such a quantity also appears in the discussion regarding the discrepancy between QE boundary conditions for binary BHs and spacetime stationarity in Ref. [65]. Its enforcement has been found to cause non-invertibility of the differential operator associated with the momentum constraint or lead to instabilities otherwise [65, 66]. We calculate this term using the identity (see, e.g., Eq. (6.70) in Ref. [67])

$$\mathcal{L}_\xi \ln \psi = \frac{1}{6} (\tilde{D}_i B^i - \alpha K) + \mathcal{L}_B \ln \psi, \quad (14)$$

where  $B^i := \beta^i + \Omega \partial_\phi^i$  is the so-called corotational shift; note that the last term in (14) appears when the divergence of the shift vector is taken with respect to the conformal spatial metric  $\tilde{\gamma}_{ij}$  as opposed to the spatial metric  $\gamma_{ij}$  as in Ref. [62]. The same equation as here is also reported, e.g., in Ref. [65, 66]. The left-hand side of Eq. (14) can be seen as a residual of the equilibrium condition  $\mathcal{L}_\xi \gamma_{ij} = 0$ , which can be written more explicitly as

$$0 = \mathcal{L}_\xi \gamma_{ij} = 4\psi^4 (\mathcal{L}_\xi \ln \psi) \tilde{\gamma}_{ij} + \psi^4 \mathcal{L}_\xi \tilde{\gamma}_{ij}. \quad (15)$$

Clearly, the choice of free data  $\mathcal{L}_\xi \tilde{\gamma}_{ij} = 0$  will only remove the second, but not the first term on the right-hand side. Therefore,  $\mathcal{L}_\xi \ln \psi$  provides a simple and yet useful estimate of the

<sup>1</sup> Note that in practice the solver uses the equations multiplied by the ratio of pressure to density  $p/\rho$  in order to improve the performance of spectral methods in the presence of matter fields.

<sup>2</sup> Under the conformal decomposition, the term  $\mathcal{L}_\xi \ln \psi$  contributes to the last term in Eq. (213) in Ref. [64].

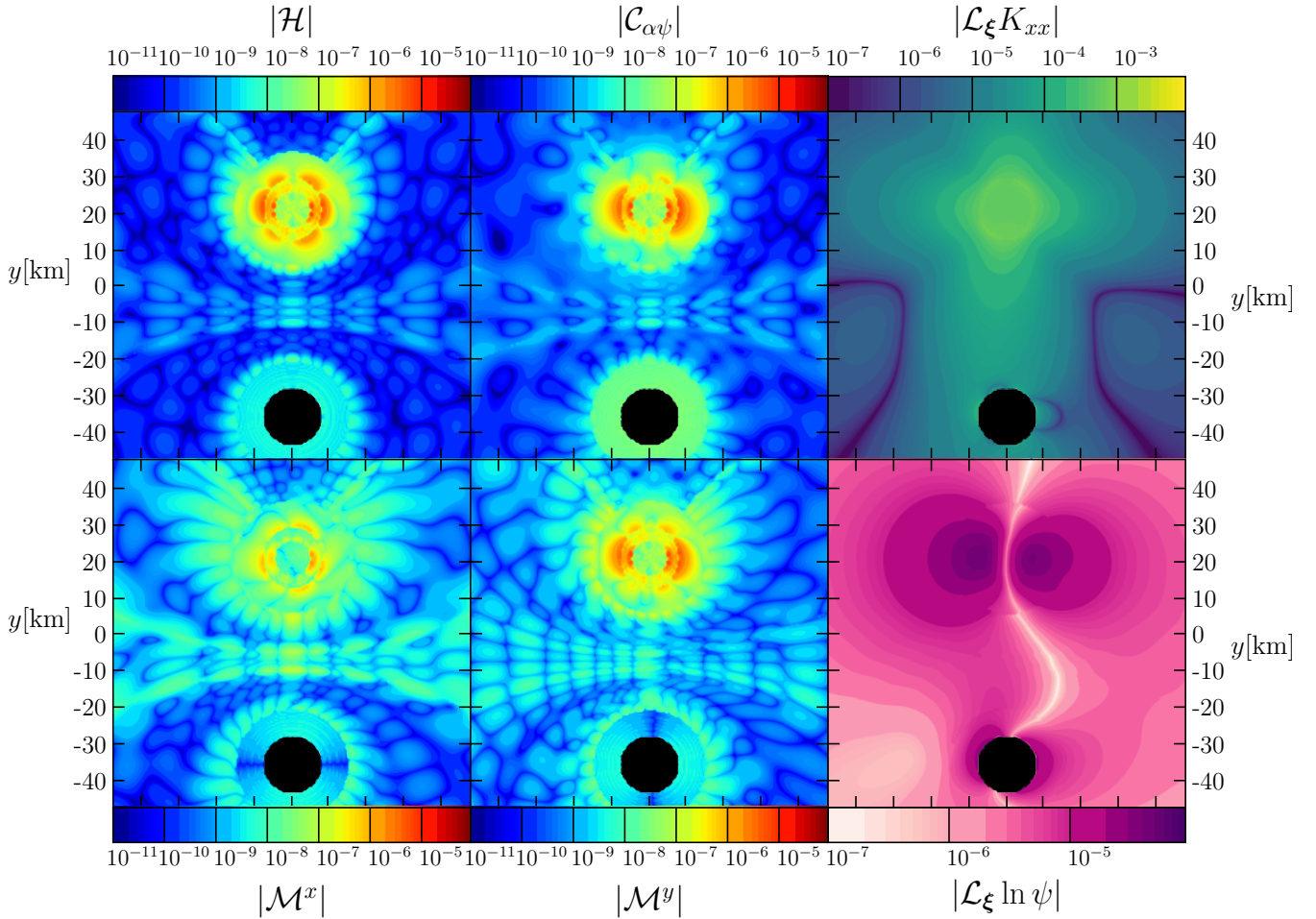


FIG. 1. The representative monitoring quantities  $\mathcal{H}$  (top-left panel),  $\mathcal{M}^x$  (bottom-left panel),  $\mathcal{C}_{\alpha\psi}$  (top-middle panel),  $\mathcal{M}^y$  (bottom-middle panel) relative to constraints Eqs. (2) – (5) of the XCTS system. The data refers to a typical BHNS configuration at a separation of  $d = 56.865$  km, with a total mass of  $7.800 M_\odot$ , where  $M_{\text{NS}} = 1.300 M_\odot$ , mass ratio  $Q := q^{-1} = 5$  and where the NS matter is modelled by the intermediate EOS. Shown in the top and bottom panels on the right are two novel monitoring quantities measuring the deviation of  $\xi$  from being a true helical Killing vector field. In all cases, black circles denote the apparent horizon of the BH.

deviation from the QE condition (see Fig. 1). A similar diagnostic quantity can be constructed by looking at the magnitude of  $\mathcal{L}_\xi K_{ij}$ , whose explicit expression can be found at the end of Appendix A. In this case, while  $\mathcal{L}_\xi K_{ij} = 0$  is not enforced explicitly (in fact, only its trace part is), since  $K_{ij}$  is a tensor of a spacetime with global helical symmetry  $\xi$ ,  $\mathcal{L}_\xi K_{ij}$  should necessarily vanish for all of its components as well<sup>3</sup>. Of course, since  $\xi$  is a helical symmetry vector of the spacetime only approximately, both of these Lie derivatives are expected to be as small as possible globally for the set of equations to be consistent with the QE assumption.

In Fig. 1 we report the constraints defined in Eqs. (2), (3) and (4), as well as the two extra diagnostics quantities (14) and (A7) as a way to judge the degree of helical symmetry in the initial data for a representative BHNS binary system.

<sup>3</sup> Note that  $\mathcal{L}_\xi g_{\mu\nu} = 0$  for a Killing vector  $\xi$  does not imply that  $\mathcal{L}_\xi K_{\mu\nu} = 0$ .

More specifically, the figure refers to an irrotational BHNS system with a separation  $d = 56.865$  km, where the NS mass (in isolation) is  $M_{\text{NS}} = 1.300 M_\odot$  and the BH Christodoulou mass is  $M_{\text{Ch}} = 6.500 M_\odot = 5 M_{\text{NS}}$ . The distance between the objects was chosen so as to show the level of constraint violations at a close proximity as measured by  $d/M_{\text{tot}} = 4.94$ . The spectral resolution used here and throughout the paper is  $N = 13$  and the definition of this spectral resolution will be discussed in Sec. III.

While the constraint equations are solved to a high degree of precision at each spectral collocation point, Fig. 1 shows the violations obtained from the spectral interpolation function for each constraint equation. Note that the interpolants for  $(\mathcal{H}, \mathcal{M}^i, \mathcal{C}_{\alpha\psi}) = \mathbf{0}$  are satisfied at an average absolute precision of  $10^{-10} - 10^{-9}$ , with violations that increase by about one order of magnitude in the vicinity of the BH, and reaching at most  $\sim 10^{-6}$  around the NS. The degree of “non-helicity” as measured by  $\mathcal{L}_\xi \ln \psi$  and  $\mathcal{L}_\xi K_{xx}$  shown in the two right-most panels is consistent with previous studies under similar



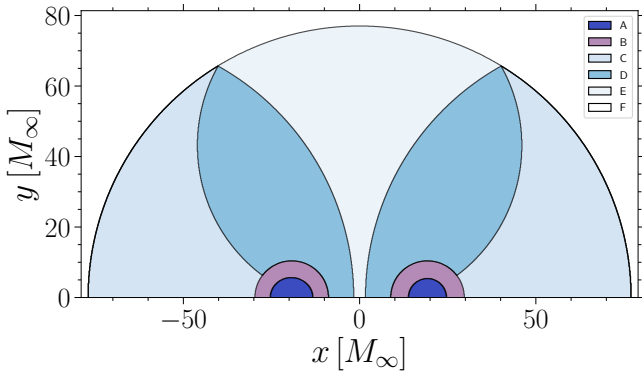


FIG. 2. Representative example of the non-overlapping domain decomposition used in FUKA for constructing BHNS initial data. The legend for the various patches is described in the text and the figure is generated using the same BHNS binary described in Fig. 1.

QE assumptions [62, 65]. Overall, the level of constraint violations shown in Fig. 1 is characteristic for all of our initial data configurations and is optimal in the sense that decreasing it further would only be possible with a considerable additional computational cost by going to higher spectral resolution. Conversely, going to higher spectral resolution can also lead to introducing spectral noise (i.e. Gibbs phenomenon) at the NS surface which can spoil the solution; therefore, a conservative spectral resolution is necessary without resorting to spectral filtering algorithms. Finally, because the example considered refers to a binary configuration at a very close separation distance, it represents an upper bound for the level of constraint violations for the binary configurations reported in this paper.

As a final remark and mostly for completeness, it is instructive to mention that conformally flat initial data with a spinning isolated BH is inherently incompatible with the axisymmetric slicing of Kerr spacetime [68–70] and effectively introduces unphysical radiation content. Techniques have been reported in the literature when constructing binary initial data that includes a BH which abandon the conformally flat approximation and, instead, compute conformally curved initial data where  $\tilde{\gamma}_{ij} \neq \delta_{ij}$  and  $K \neq 0$ . Conformally curved BHNS initial data has previously been constructed using the modified-Kerr-Schild conformal metric [45, 62, 71], based on the previous super-imposed Kerr-Schild data [72] for BBH systems. While Ref. [38] used the Kerr-Schild representation of the Schwarzschild metric, only irrotational sequences were considered there. Finally, it is worth noting that although techniques exist in the literature for constructing conformally curved initial data, no public code exists with these capabilities with the exception being the elliptic solver in SpECTRE for generating conformally curved BBH initial data [73, 74].

### III. NUMERICAL SETUP

#### A. The FUKA code

The results presented here have been obtained with the open-source and publicly available FUKA code, which is a suite of initial-data solvers designed to compute initial conditions for isolated and binary compact objects, with a focus on highly mass asymmetric and spinning configurations. FUKA is built on an extended version of the KADATH spectral-solver library which is a highly-scalable, MPI-parallelized, C++ library specifically designed for numerical relativity problems [61]. To discretize the physical space, KADATH utilizes a multi-grid approach where multiple non-overlapping grids are used which are chosen based on the problem being solved. Figure 2 illustrates the domain decomposition for BHNS initial data. Regions A (right) denote the excised region of the BH or (left) the stellar interior. The boundaries between regions A and B are adaptive and are not required to remain spherical. Instead, they are specifically designed to adapt to the surface of a problem which, in this case, is the apparent horizon radius dictated by the irreducible mass of the BH or the deformation of the NS surface. It is important to note that the latter is sensitive not only to the mass and spin of the NS, but also the tidal deformations that result from computing initial data with small separation distances (i.e.,  $d/M_{\text{tot}} \lesssim 6$ ). Secondly, although not shown for this particular initial data, region B can include additional spherical shells to provide local refinement without increasing the spectral resolution. This is extremely important for BHNS systems with  $M_{\text{Ch}} \ll 5 M_{\text{NS}}$  and  $|\chi_{\text{BH}}| \gg 0$  for which the excised region becomes increasingly smaller than the NS radius [48, 53]. Region F consists of the outermost spherical shell that utilizes a compactified radial coordinate. Finally, regions C, D, and E form a bispherical decomposition that provides a continuous chart between the outermost spherical boundary of each compact object and the compactified outer domain. Currently, each spectral domain consists of the same number of collocation points in the  $r$ ,  $\theta$ , and  $\phi$  directions. Here, we define a resolution  $N$  such that the spectral resolution in  $(r, \theta, \phi)$  is  $(N, N, N - 1)$ .

The system of elliptic equations is solved across all domains consistently using a standard Newton-Raphson method where each iteration attempts to minimize the residual error. Elliptic solvers that utilize Jacobian methods tend to suffer from convergence issues as convergence is heavily dependent on the quality of the initial “guess” used for the first iteration. FUKA takes an iterative complexity approach to build the initial guess from boosted isolated solutions using the XCTS system of equations to maximize the likelihood of convergence [48]. Additionally, the boosted isolated solutions provide valuable information as to whether additional spherical shells in region B are needed to ensure sufficient resolution is available to resolve small features, such as the BH apparent horizon, without resorting to globally increasing the spectral resolution. At the same time, the surface of the NS is challenging to model with spectral methods as it introduces a natural discontinuity that is a common source of spectral noise known

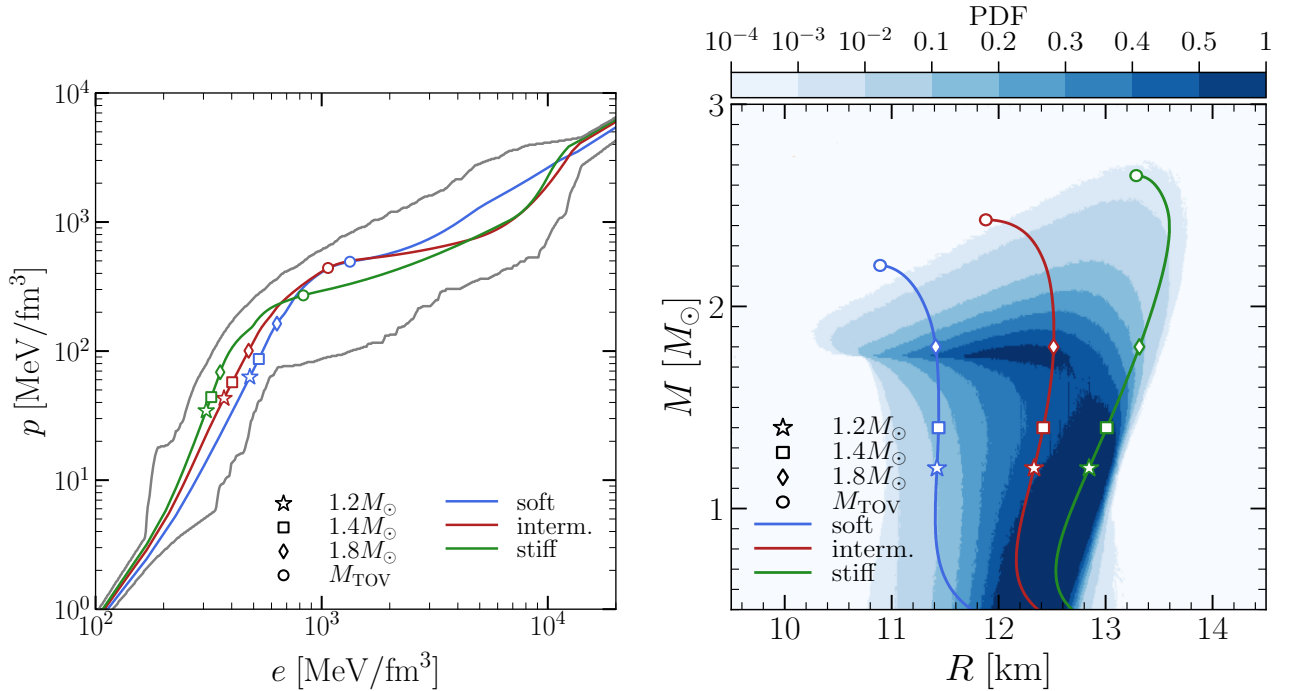


FIG. 3. *Left panel:* the pressure and energy density profiles for the soft (blue solid line), intermediate (red solid line) and stiff (green solid line) EOSs, respectively, utilized in this work. Shown instead with grey contours are the ranges of pressures and energy densities within which the EOSs are admissible under chiral-field theory, perturbative quantum chromodynamical (QCD) constraints, and astronomical observations. *Right panel:* the same EOSs as in the left panel, but shown in terms of the  $M$ - $R$  curves for nonrotating stellar models.

as ‘‘Gibbs phenomenon’’. Here, we minimize the spectral noise in the numerical methods in two ways. First, KADATH implements a non-overlapping multi-grid scheme and, therefore, the spectral solution in a given domain describes only the local solution within that domain with appropriate boundary conditions ensuring the solution in one domain matches the solution in the neighbouring domain. Secondly, we use a conservative resolution of  $N = 13$ , which has shown to provide robust solutions (see Fig.1) without introducing excessive spectral oscillations at the NS surface. We have checked that the quantities needed for the analysis as well as general diagnostics are already robust at this resolution and no notable change is present when the resolution is increased. The overall convergence properties of FUKA have been demonstrated previously in [58]. For the quantities needed in our current analysis, the differences measured when increasing the resolution to  $N = 15, 17, 19$  are below 0.5% for  $\kappa$  and 0.1% for  $E_b$  (see below for a definition). The differences at  $N = 13, 15, 17$  computed with respect to  $N = 19$  also decrease with resolution, signalling convergence.

Furthermore, it is worth mentioning that due to the choice of spectral bases in KADATH, only spins aligned or anti-aligned with the orbital angular momentum are possible. It has been found, however, that the crucial quantity in determining the outcome of the merger is the projection of the BH spin vector orthogonal to the orbital plane, i.e.,  $\chi_{\text{BH}} \cdot \hat{z}$  [71, 75]. For that reason, we expect the results we obtained using  $\chi_{\text{BH}} = \chi_{\text{BH}} \hat{z}$  to be qualitatively robust and representative even for more generic configurations. We leave it to future

work to explore the potential impact misaligned spins may have when analysing equilibrium initial data sequences in a similar manner.

Finally, to ensure a comprehensive and model-agnostic coverage of the parameter space of EOSs describing NS matter, we choose three representative EOSs from an ensemble generated by uniform sampling with the speed-of-sound parametrization (see [76, 77] for details). The radius measurements of NICER [78–81] and the upper bound on the binary tidal deformability as measured for GW170817 by the LIGO/Virgo collaboration [82] have been imposed to reject EOSs that violate these measurements. In the left panel of Fig. 3 we show the pressure as a function of energy density  $p(e)$  for these three EOSs. Each colour corresponds to a different stiffness of the EOS, where blue is for the soft EOS, green is for the stiff EOS and red is for the EOS of intermediate stiffness. Furthermore, pressure and energy density values at the centre of the NS ( $p_c, e_c$ ) corresponding to ADM masses of the NSs of  $1.2, 1.4, 1.8 M_{\odot}$ , as well as to the Tolman-Oppenheimer-Volkoff mass  $M_{\text{TOV}}$  representing a nonrotating star of maximal admissible ADM mass are marked with symbols. In addition, grey contours are added indicating the ranges of pressures and energy densities where the EOSs are admissible under chiral-field theory, perturbative quantum chromodynamical (QCD) constraints, and astronomical observations. Clearly, the EOSs chosen roughly trace the outer contours of the probability distribution of said ensemble, as well as the highest likelihood region and are collectively presented in the right panel of Fig. 3 (see Ref. [83] for a

more sophisticated approach for the selection of the EOSs by exploiting a principal-component analysis of the stellar properties).

### B. Mass-shedding frequency and binding energy

The sequences of QE binaries we consider here are characterized by constant values of the NS baryon rest mass  $M_b$ , the dimensionless spins of the two components  $\chi_{\text{BH/NS}}$ , a fixed EOS, and by the BH Christodolou mass

$$M_{\text{Ch}}^2 := M_{\text{irr}}^2 + \mathcal{S}^2/4M_{\text{irr}}^2;$$

where  $M_{\text{irr}}$  is the irreducible mass of the BH and  $\mathcal{S}$  the spin angular momentum measured on the apparent horizon. In FUKA, the BH is excised from the computational domain and the excision boundary is enforced to be an apparent horizon. As such, the Christodolou mass provides a robust measurement of the BH gravitational mass even in a binary configuration as the spin angular momentum and the irreducible mass have well defined geometric definitions [58]. A NS, however, does not have a well-defined measurement of its gravitational mass in the presence of a companion object. Instead, the ADM mass of the NS is computed and fixed at infinite separation (i.e., in isolation) and, thereafter, the baryon rest mass will remain constant along the sequence, mimicking dynamical evolution through QE slices. Individual datasets along a sequence are parameterized either by the coordinate separation or by the orbital angular velocity, which is part of the solution. With  $M_b$  constant and thus always representing the same star, each sequence is also uniquely defined by the value of the NS compactness  $\mathcal{C} := M_{\text{NS}}/R_{\text{NS}}$  as computed in isolation<sup>4</sup>. For a BHNS configuration at a given separation, we compute two important quantities necessary for our analysis. Following Ref. [40], we first define the *mass-shedding* diagnostic as the ratio of the slope of the log specific enthalpy  $h$  along the equatorial and polar direction

$$\kappa := \frac{\partial_r \ln h|_{\text{eq}}}{\partial_r \ln h|_{\text{pole}}}. \quad (16)$$

Such a quantity is a sensitive indicator of the NS deformation resulting from the presence of tidal forces. Clearly,  $\kappa = 1$  for a spherical star (hence in isolation) while the formation of a cusp on the NS surface can be taken as the limit in which  $\kappa \rightarrow 0$ , which would indicate the onset of mass shedding. Because our solver uses spectral methods to compute the initial data and hence cannot handle any sharp features, the computed sequences do not extend to the mass-shedding value of 0 and reach  $\sim 0.5$  at their smallest instead (a similar approach was followed also in Ref. [40]).

<sup>4</sup> Sequences of constant quasi-local ADM mass for the NS do not represent a useful option due to systematic deviations [84]. Here,  $R_{\text{NS}}$  is the NS areal radius and  $M_{\text{NS}}$  its ADM mass. Therefore, for clarity and with no risk of confusion, throughout the paper we shall always use  $M_{\text{NS}}$  to denote the isolated NS ADM mass.

The second important quantity in our analysis is the *binding energy*, also referred to as the *effective potential* (e.g., [85]), defined as

$$E_b := M_{\text{ADM}} - M_{\text{tot}}, \quad (17)$$

where  $M_{\text{ADM}}$  is the ADM mass of the hypersurface calculated according to Eq. (12) and we define the (isolated) total mass simply as

$$M_{\text{tot}} := M_{\text{NS}} + M_{\text{Ch}}. \quad (18)$$

In analogy to the role played by the effective potential in determining the existence and stability of circular orbits in BH spacetimes, the minimum of the binding energy provides a working definition for the location of the *marginally stable* orbit in the spacetime relative to the BHNS binary. In this work it was often found necessary to extrapolate  $E_b$  to locate this minimum. This point and its implications will be discussed in detail in Sec. IV.

### C. Tidal forces analysis in the initial data

Next, we briefly present a new approach to study tidal forces in numerically generated spacetimes that is complementary to the one presented in the previous section in terms of the mass-shedding quantity  $\kappa$ . To the best of our knowledge, and leaving aside the analytical approaches discussed in Refs. [24, 86–88] which make use of tidal force analysis in a convenient reference frame, this is the first time this approach is proposed and employed for BHNS sequences.

The starting point of our analysis is represented by the equation of geodesic deviation that characterises the influence of spacetime curvature on the separation of neighbouring geodesic curves along a congruence. Denoting the second covariant derivative along the direction of the geodesic four-vector field  $\mathbf{u}$  by  $D^2/D\tau^2$ , the spacetime Riemann tensor by  $\mathbf{R}$  and the separation four-vector by  $\mathbf{X}$ , the relevant equation reads

$$\frac{D^2 X^\mu}{D\tau^2} = R^\mu{}_{\alpha\beta\gamma} u^\alpha u^\beta X^\gamma, \quad (19)$$

We now introduce a tetrad, i.e., a set of orthonormal vectors  $\{\mathbf{e}_{\hat{a}}\}$  with  $g_{\mu\nu} e_{\hat{a}}^\mu e_{\hat{b}}^\nu = \eta_{\hat{a}\hat{b}} = \text{diag}(-1, 1, 1, 1)$ , with tetrad indices marked by hatted Latin indices  $\hat{a} = \{0, 1, 2, 3\}$  and with  $\eta_{\hat{a}\hat{b}}$  the Minkowski metric. Assuming now that the tetrad is parallelly propagated along the geodesic field, i.e.,  $\nabla_{\mathbf{u}} e_{\hat{a}} = 0$ , where  $e_{\hat{0}} = \mathbf{u}$  and with  $\hat{a} = \{1, 2, 3\}$  for some spacelike unit vectors  $e_{\hat{a}}$  at each event, a useful simplification of the geodesic deviation equation is achieved. Namely, the left-hand side simplifies to an ordinary second derivative of the components of the deviation vector expressed in the frame basis; in addition, the evolution of the timelike component  $X^{\hat{0}}$  becomes trivial. Indeed, for a decomposition of the separation vector in the frame basis

$$\mathbf{X} = X^{\hat{0}} \mathbf{e}_{\hat{0}} + X^{\hat{i}} \mathbf{e}_{\hat{i}}, \quad (20)$$

one finds by writing the covariant derivative in full

$$\nabla_{e_0} \mathbf{X} = \frac{dX^{\hat{0}}}{d\tau} e_{\hat{0}} + X^{\hat{0}} \nabla_{e_0} e_{\hat{0}} + \frac{dX^{\hat{i}}}{d\tau} e_{\hat{i}} + X^{\hat{i}} \nabla_{e_0} e_{\hat{i}}, \quad (21)$$

where the second and the fourth term vanish. Applying the covariant derivative a second time, thus yields

$$\frac{D^2 \mathbf{X}}{D\tau^2} = \frac{d^2 X^{\hat{0}}}{d\tau^2} e_{\hat{0}} + \frac{d^2 X^{\hat{i}}}{d\tau^2} e_{\hat{i}}. \quad (22)$$

The right-hand side of Eq. (19) in the tetrad basis becomes  $R^{\hat{a}}_{\hat{0}\hat{b}} X^{\hat{b}}$ , which vanishes for  $\hat{a} = 0$  due to the symmetries of the Riemann tensor. The general solution for the time component is then readily obtained as  $X^{\hat{0}} = \lambda_1 \tau + \lambda_2$  for some constants  $\lambda_1, \lambda_2$ .

Defining now the ‘‘tidal-force operator’’ to be a 3-by-3 symmetric matrix given by  $C_{\hat{i}\hat{j}} = \mathbf{R}(e_{\hat{i}}, \mathbf{u}, \mathbf{u}, e_{\hat{j}}) = R_{\hat{i}\hat{0}\hat{0}\hat{j}}$ , the remaining spatial components of the geodesic-deviation equation in a parallelly propagated frame amount to [cf., Eq. (3.11) in [89]]

$$\frac{d^2 X_{\hat{i}}}{d\tau^2} = C_{\hat{i}\hat{j}} X^{\hat{j}}. \quad (23)$$

While this choice of frame is a particularly convenient one, it requires the solution of both the geodesic equation for the first vector of the tetrad, i.e.,  $e_{\hat{0}}$ , and the solution of the equations of parallel transport along  $e_{\hat{0}}$  for the remaining vectors  $e_{\hat{a}}$  of the tetrad. Furthermore, because the fluid motion is not geodesic as a result of pressure gradients, a nonzero acceleration  $\mathbf{a} := \nabla_{\mathbf{u}} \mathbf{u}$  will be present and would manifest via additional terms on the right-hand side of the geodesic deviation equation (19) (see, e.g., [89] for more details). On the other hand, the failure to parallel transport the remaining spacelike tetrad vectors in Eq. (23) would contribute extra terms involving Christoffel symbols that account for the Coriolis force due to the absence of Fermi-Walker transport and present for a rotating reference frame. To cope with these shortcomings and develop an approach that is better suited to our initial data, we here choose the spatial vectors of our tetrad to be simple unit Cartesian coordinate vectors and accordingly refer to the *effective* ‘‘tidal-force operator’’ of the *generic* tetrad  $\{e_{\hat{a}}\}$  as the contraction of the Riemann tensor with the timelike vector field of the frame defined above. In addition, rather than working with a (spatial) rank-two tensor  $C_{\hat{i}\hat{j}}$ , which is dependent on the choice of spatial tetrad vectors, we will instead look at its (spatial) contraction  $C_{\hat{i}\hat{j}} C^{\hat{i}\hat{j}}$ , which is a scalar field.

More specifically, hereafter we will consider the frame associated with an observer comoving with the fluid and, within a 3+1 decomposition of spacetime, we express the fluid four-velocity  $u^\mu = W(n^\mu + U^\mu)$ , with  $W$  the Lorentz factor,  $n^\mu$  the unit time-like normal to the spacelike hypersurface, and  $U^\mu$  the 3-velocity obtained by the projection onto the hypersurface [41]. The tidal-force operator in such a frame then reads

$$\begin{aligned} C_{\hat{i}\hat{j}} &= \mathbf{R}(e_{\hat{i}}, \mathbf{u}, \mathbf{u}, e_{\hat{j}}) \\ &= W^2 [\mathbf{R}(e_{\hat{i}}, \mathbf{n}, \mathbf{n}, e_{\hat{j}}) + \mathbf{R}(e_{\hat{i}}, \mathbf{n}, e_{\hat{k}}, e_{\hat{j}}) U^{\hat{k}} \\ &\quad + \mathbf{R}(e_{\hat{j}}, \mathbf{n}, e_{\hat{k}}, e_{\hat{i}}) U^{\hat{k}} + \mathbf{R}(e_{\hat{i}}, e_{\hat{k}}, e_{\hat{l}}, e_{\hat{j}}) U^{\hat{k}} U^{\hat{l}}], \end{aligned} \quad (24)$$

where the third term involving a single contraction with the  $n^\mu$  vector has been permuted using the symmetry of the fully covariant Riemann tensor (i.e.,  $R_{\alpha\beta\gamma\delta} = R_{\delta\gamma\beta\alpha}$ ). The necessary projections of the spacetime Riemann tensor along the normal and spatial directions in terms of the 3+1 variables are listed in the Appendix A along with the reconstruction procedure.

In the top panels of Fig. 4 we present the tidal-force scalar  $\Upsilon := C_{\hat{i}\hat{j}} C^{\hat{i}\hat{j}}$  for BHNS binaries having different BH spins  $\chi_{\text{BH}}$  (see top left corner of each panel) and for a fixed separation  $d$ . For this analysis we utilize the intermediate stiffness EOS, we fix the ADM mass of the NS to  $M_{\text{NS}} = 1.328 M_\odot$  and fix the mass ratio to  $Q := q^{-1} = 4$ . Similarly, in the bottom panels we report the same scalar quantity, but for binaries having  $\chi_{\text{BH}} = 0$  and different values of the binary separation  $d/M_\odot \in \{33.1, 36.0, 38.0\}$  and corresponding orbital angular velocities  $\Omega M_\odot \in \{0.01046, 0.00940, 0.00877\}$ . Also reported in each panel is the ratio of the NS semi-axes as measured in the polar direction and in the direction of the BH  $\mathcal{R} = a_{\text{pole}}/a_{\text{eq}}$  (see bottom right corner of each panel). Note that rather than showing  $C_{\hat{i}\hat{j}} C^{\hat{i}\hat{j}}$  for each configuration, in some of the panels we report the normalised difference between two configurations, i.e.,  $(\Upsilon - \Upsilon_0)/(\Upsilon + \Upsilon_0)$ , where the subscript 0 refers to the one at zero BH spin (top panels) or the intermediate distance (bottom panels). Using this quantity, it is easier to appreciate that the tidal forces undergo largest changes in the outer layers of the NS and that the maximum value of  $C_{\hat{i}\hat{j}} C^{\hat{i}\hat{j}}$ , located at the centre of the NS, increases by around 2% in the counter-rotating BH case when compared to the co-rotating one. A similar behaviour is observed in the lower panels, where a decrease in the binary separation is clearly accompanied by an increase in the tidal force in the outer layers of the NS, orthogonal to the line connecting the two objects (indicated by the red regions), with a less prominent decrease closer to the core (in blue)<sup>5</sup>. The maximum of  $C_{\hat{i}\hat{j}} C^{\hat{i}\hat{j}}$  grows by 0.1% between the largest and the smallest separations. The axis-ratio, on the other hand, decreases by  $\sim 0.02$  between two consecutive separations. Interestingly, when comparing across top and bottom panels in Fig. 4 we observe that changing the spin from  $\chi_{\text{BH}} = 0.8$  to  $\chi_{\text{BH}} = -0.8$  at a fixed separation causes a change to the NS shape of a similar magnitude as to when the separation decreases by  $\sim 7.5$  km. On a more formal level, we note that the comparison made above is based on coordinate descriptions that vary from configuration to configuration. Hence, differences in  $\Upsilon$  could be simply the result of the different gauges and not be physical. However, given that the gauges are very similar in all the examples considered, we expect that  $\Upsilon$  depends on the used gauges only weakly across different binaries. Hence, we expect the results discussed to be correct, at least at a qualitative level. A more rigorous comparison for datasets at different separations would be in principle possi-

<sup>5</sup> Individual components of  $C_{\hat{i}\hat{j}}$  may display different longitudinal and transverse changes, but the full contraction  $\Upsilon$  manages to provide the basic and generic behaviour.



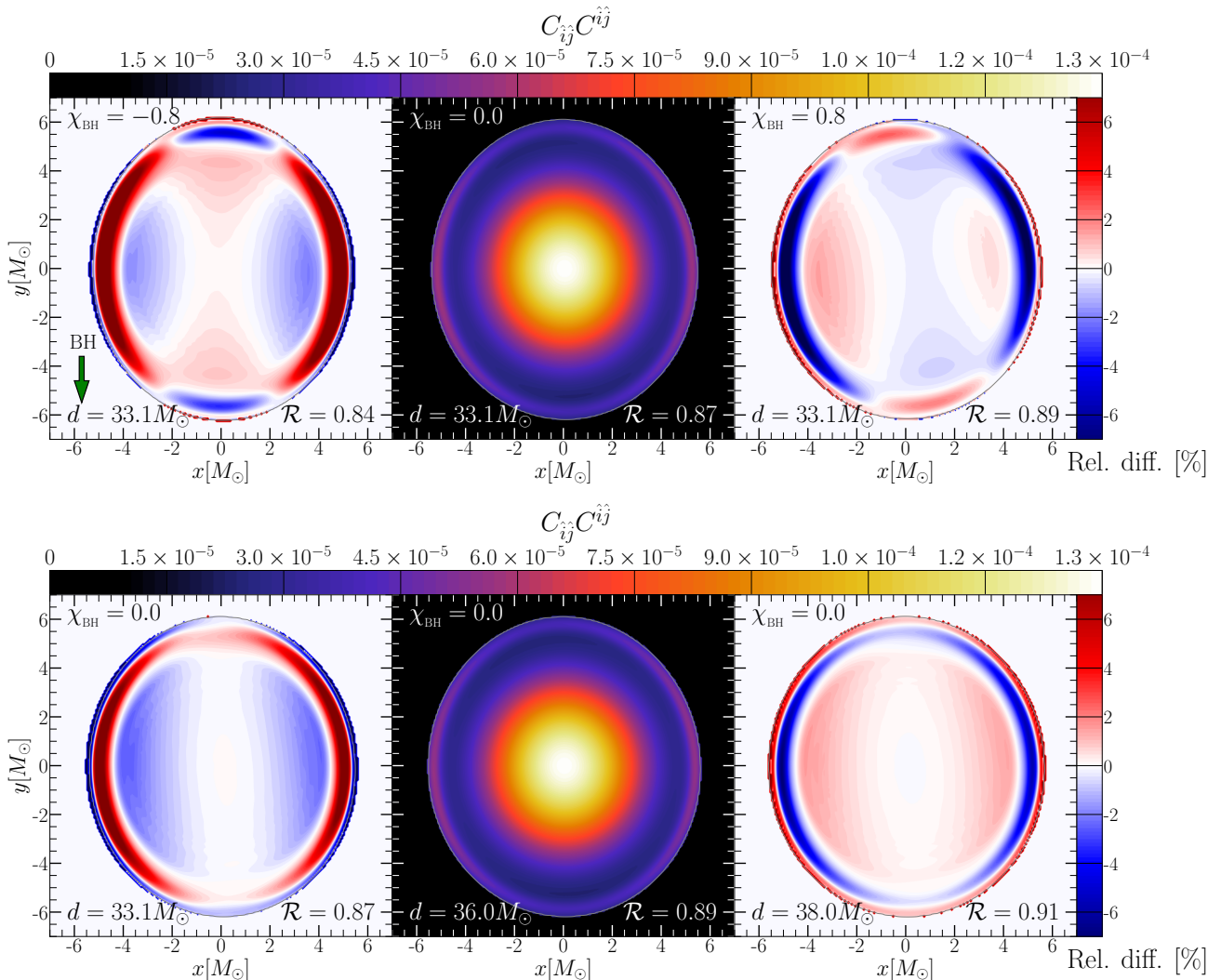


FIG. 4. Representative examples of the monitoring quantity  $\Upsilon := C_{ij}^{\ddot{}} C^{ij}$ , with  $C^{ij}$  [see Eq. (24) for a definition] for BHNS binaries relative to a mass ratio  $Q = 4$ , a total mass  $M_{\text{tot}} = 6.640 M_{\odot}$  and the EOS of intermediate stiffness; the green arrow points in the direction of the BH. *Top panels:* tidal-force indicator  $\Upsilon$  for different BHNS binaries having the same separation of  $d/M_{\odot} = 33.1$  but different BH spin (i.e.,  $\chi_{\text{BH}} = -0.8, 0, 0.8$ , respectively). The top-left and top-right panels actually refer to the relative difference  $(\Upsilon - \Upsilon_0)/(\Upsilon + \Upsilon_0)$  with respect to the middle panel, with  $\chi_{\text{BH}} = 0$  (i.e.,  $\Upsilon_0$ ) to help appreciate the differences across the sequence. Note that the largest distortions take place near the stellar surface and in a rather thin region. *Bottom panels:* the same as on the top but for BHNS binaries having the same spin  $\chi_{\text{BH}} = 0.0$  but different separations (i.e.,  $d/M_{\odot} = 33.1, 36.0, 38.0$ , respectively). Also in this case, the central panel shows  $\Upsilon$  while the left and right panels illustrate the relative difference  $(\Upsilon - \Upsilon_0)/(\Upsilon + \Upsilon_0)$ .

ble when considering points along integral curves of  $\xi$  and where  $\xi$  is to follow some evolutionary constraints that mimic dynamical evolution (see, e.g., [90] for a related example). Such a comparison, which, to the best of our knowledge, has not been explored so far, would still be approximate, but it would reduce the role of local gauges across different QE sequences.

We note that the behaviour illustrated above can be also described in terms of the orbital angular velocity or the axis ratio. In particular, the change in  $\Omega$  is  $\delta\Omega M_{\odot} = 0.00097$  between the most extreme spins in the upper panels, while  $\delta\Omega M_{\odot} = 0.00169$  when changing separations in the lower panel. At the same time, the difference in  $\mathcal{R}$  between  $\chi_{\text{BH}} = \pm 0.8$  is larger by 0.01 than the difference in the lower panel, in spite of a

smaller change in  $\delta\Omega$  between these configurations. In other words, the change in separation involves a larger change in  $\delta\Omega$  and yet a smaller one in the deformation  $\delta\mathcal{R}$ . This is because the tidal deformations are affected more severely by a change in the BH spin than by the binary separation for the inspected spins and distances. Furthermore, the greatest tidal forces and most prominent deformation of the NS are present when the spin of the BH is in the opposite direction to the orbital angular velocity of the system (i.e., a BH with anti-aligned spin). The analogy to non-relativistic physics is easily made if we recall that frame dragging effectively introduces an additional force on test particles, with the sense of direction dictated by the BH spin. Hence, the combination of orbital motion of the fluid with the frame dragging induced by a counter-rotating

BH is responsible for the greatest degree of deformation and the largest tidal forces. Interestingly, in spite of a different choice for our tetrad, the phenomenology described so far in terms of the tidal-force scalar is consistent with the analytical predictions dating back to [86] and that made use of a parallelly-transported tetrad derived in [91]. In the accompanying paper II [57], we will present the evolution of the scalar  $\Upsilon$  in a fully dynamical setup.

As a final remark we note that even though the inspection of tidal forces in a suitable frame provides a considerable amount of insight into the forces and deformations taking place within the NS matter, we will not employ it hereafter to determine the onset of the mass-shedding or to localize the marginally stable orbit. Rather, in order to maintain consistency with previous literature and compare directly to published results, the remainder of this work will employ the diagnostics presented in Sec. III B in terms of the dimensionless radial deformation  $\kappa$  and of the binding energy  $E_b$ .

#### IV. RESULTS

In what follows, we present our results for QE sequences of BHNS binaries in quasi-circular orbits and from which we will estimate the values of the mass-shedding frequency  $\Omega_{\text{MS}}$  and of the innermost stable circular orbit  $\Omega_{\text{ISCO}}$  as defined in Sec. III.

##### A. Polytropic EOS and comparison with literature

Before we embark on the discussion of QE sequences using realistic EOSs, it is useful to test the performance of the FUKA code by comparing its results with those published in the literature. In this case, the most exhaustive analysis is that offered by Taniguchi and collaborators [40], who have considered QE sequences of BHNS binaries when the neutron-star matter is modelled with a simple polytropic EOS with adiabatic index  $\Gamma = 2$  (i.e., an  $n = 1$  polytrope). For the purpose of comparison, we fix the ADM masses of the NSs (and thus the compactnesses) to those employed in [40]. The values of the used ADM masses in isolation and those of the baryonic rest-masses, of the areal radii, compactnesses, and the central values of the rest-mass densities and pressures are listed in Tab. I. The mass ratio is chosen depending on the compactness of the constant rest-mass sequence and ranges between  $Q = 1$  and  $Q = 10$ . The rest-mass values are uniformly spaced between  $1.3 M_\odot$  and  $1.7 M_\odot$ .

In Fig. 5 we compare the results of our analysis for  $\kappa$  (top panel) and  $E_b$  (bottom panel) with those of Ref. [40]. For brevity, only the QE sequences with rest-mass  $M_b = 1.5 M_\odot$  and mass ratios  $Q = 1, 2, 3, 5$  are reported. Note that we find excellent agreement along the sequences both in the mass-shedding indicator and the binding energy, with differences that appear only at the highest frequencies, where our solutions managed to reach somewhat larger values. These differences, however, are much smaller than the ones that have been

EOS	$M_{\text{NS}}$ [ $M_\odot$ ]	$M_b$ [ $M_\odot$ ]	$R_{\text{NS}}$ [km]	$\mathcal{C}$	$10^3 \times \rho_c$ [ $M_\odot^{-2}$ ]	$10^4 \times p_c$ [ $M_\odot^{-2}$ ]
$\Gamma = 2$	1.223	1.300	15.050	0.120	0.914	0.835
	1.310	1.400	14.658	0.132	1.073	1.152
	1.395	1.500	14.210	0.145	1.256	1.578
	1.478	1.600	13.650	0.160	1.495	2.236
	1.560	1.700	12.944	0.178	1.893	3.582
soft	1.200	1.311	11.301	0.157	1.295	1.835
	1.400	1.557	11.339	0.182	1.402	2.524
	1.800	2.080	11.345	0.234	1.633	4.743
intermediate	1.200	1.303	12.184	0.146	1.005	1.248
	1.300	1.423	12.240	0.157	1.043	1.442
	1.400	1.545	12.300	0.168	1.083	1.667
	1.800	2.052	12.429	0.214	1.247	2.903
stiff	1.200	1.299	12.688	0.140	0.845	0.998
	1.400	1.538	12.875	0.161	0.885	1.275
	1.800	2.038	13.220	0.201	0.957	1.985

TABLE I. Properties of the isolated NS described with the  $\Gamma = 2$  polytrope and the three realistic EOSs considered in this work. Listed for reproducibility are the ADM mass  $M_{\text{NS}}$ , the baryonic mass  $M_b$ , the areal surface radius  $R_{\text{NS}}$ , the compactness  $\mathcal{C}$ , the central density  $\rho_c$ , and the central pressure  $p_c$ .

noted in similar sequences, e.g., for  $\mathcal{C} = 0.15$  in [42], where the whole sequence is slightly shifted.

Note that since the sequences end before encountering the mass-shedding frequency (the iterative steps of the solution fail to converge at the highest orbital frequencies), an extrapolation of the computed data is necessary to extract  $\Omega_{\text{MS}}$ . To this end we resort to a functional fitting that ensures the validity of the asymptotic limit at infinite separation, i.e.,  $\kappa(\Omega) = 1$  in the limit of  $\Omega \rightarrow 0$  instead of extrapolating from the last three data points of  $\kappa$  with a quadratic polynomial as is suggested in [40]. More specifically, we perform a global fit of the computed data with a functional ansatz of the type

$$\kappa_{\text{fit}}(\Omega) = 1 + a_1 \Omega^2 \sinh(-a_2 \Omega), \quad (25)$$

where data points are not weighted equally in the fit, but with a growing weight  $w(\Omega) = \Omega$  to favour the points at the interesting end of the sequence, and set the mass-shedding frequency from the condition

$$\kappa_{\text{fit}}(\Omega_{\text{MS}}) = 0. \quad (26)$$

In this way, we find that for the less challenging configurations this ansatz (25) provides almost identical results to the usual extrapolation with a quadratic function on the last three points and meaningful (i.e., not excessively large) values of  $\Omega_{\text{MS}}$  even if the sequence ends at  $\kappa \approx 0.75 - 0.8$ .

It is often the case that the calculation of the ISCO frequency also requires a functional fitting and extrapolation as most of the QE sequences do not always reach the orbital frequencies where a minimum of the binding energy can be measured. This happens, for instance, for QE sequences having small values of  $Q$ , where cusp formation starts before the ISCO is encountered, i.e.,  $\Omega_{\text{MS}} < \Omega_{\text{ISCO}}$  (see the sequence with  $Q = 2$  in Fig. 5). On the other hand, the  $Q = 5$  sequence clearly ends with a measurable minimum in the binding energy. Hence, we choose a functional ansatz for the binding

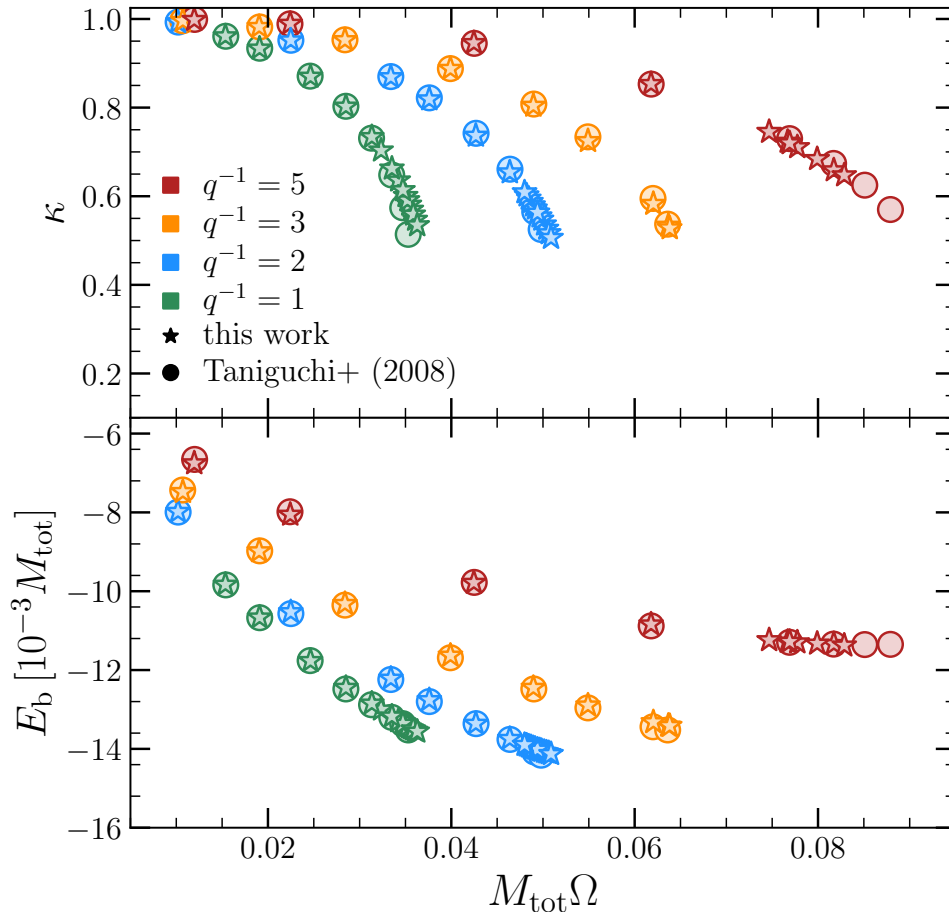


FIG. 5. *Top panel*: mass-shedding indicator  $\kappa$  [see Eq. (16) for a definition] along BHNS sequences of constant mass ratio  $Q = 1, 2, 3, 5$  and NS mass  $M_{\text{NS}} = 1.395 M_{\odot}$  when using a  $\Gamma = 2$  polytrope. Indicated with stars of different colours are the data computed here and with circles the results presented in Ref. [40]. Clearly, the agreement is very good for most of the data points. *Bottom panel*: the same as in the top panel but for the binding energy  $E_b$ .

energy that respects the asymptotic limit, i.e.,  $E_b(\Omega) = 0$  in the limit of  $\Omega \rightarrow 0$

$$E_{b,\text{fit}}(\Omega) = b_1 \Omega + b_2 \Omega^2, \quad (27)$$

and define the ISCO frequency from the condition

$$\left. \frac{\partial E_{b,\text{fit}}}{\partial \Omega} \right|_{\Omega_{\text{ISCO}}} = 0. \quad (28)$$

Examples of the fitting functions (25) and (27) can be seen as solid gray lines in the two panels of Fig. 10, which we will discuss further below.

### B. $\Omega_{\text{MS}}$ and $\Omega_{\text{ISCO}}$ : dependence on $q$ , and $\mathcal{C}$

In this section we present an intermediate investigation of the functional dependencies  $\Omega_{\text{ISCO}} = \Omega_{\text{ISCO}}(Q, \mathcal{C})$  and  $\Omega_{\text{MS}} = \Omega_{\text{MS}}(Q, \mathcal{C})$  [we recall that  $Q := M_{\text{BH}}/M_{\text{NS}} = 1/q$ ] based on the initial results presented in Sec. IV A and illustrated in Fig. 5. This analysis will be continuously elaborated

upon and extended in the following sections as we detail the results from our investigation to determine the orbital angular velocities at the ISCO  $\Omega_{\text{ISCO}}$  and at mass-shedding  $\Omega_{\text{MS}}$  for a variety of mass ratios and compactnesses. Our analysis of the irrotational QE sequences suggests a simple analytical form for  $\Omega_{\text{ISCO}}(Q, \mathcal{C})$  and  $\Omega_{\text{MS}}(Q, \mathcal{C})$  for which we propose the following expressions

$$M_{\text{tot}} \Omega_{\text{MS}}(Q, \mathcal{C}) := c_1 \mathcal{C}^{3/2} (1+Q) (1+1/Q)^{1/2} \times (1+c_2 \mathcal{C})(1+c_3 Q), \quad (29)$$

$$M_{\text{tot}} \Omega_{\text{ISCO}}(Q, \mathcal{C}) := 6^{-3/2} (1+d_1/Q^{d_2}) (1+d_1 \mathcal{C}^{d_3}/Q), \quad (30)$$

where terms in dark blue denote necessary contributions that stem from the test-particle limit in Kerr spacetime (for  $\Omega_{\text{ISCO}}$ ) or follow from the equality between the self-gravity force of the NS and tidal force from the BH in Newtonian gravity (for  $\Omega_{\text{MS}}$ ). The constants  $c_1, c_2, c_3, d_1, d_2, d_3$  are free parameters to be fitted. The terms in black in Eqs. (30) and (29) have been introduced to refine the dependence of the mass ratio and compactness to better match the numerical data and to

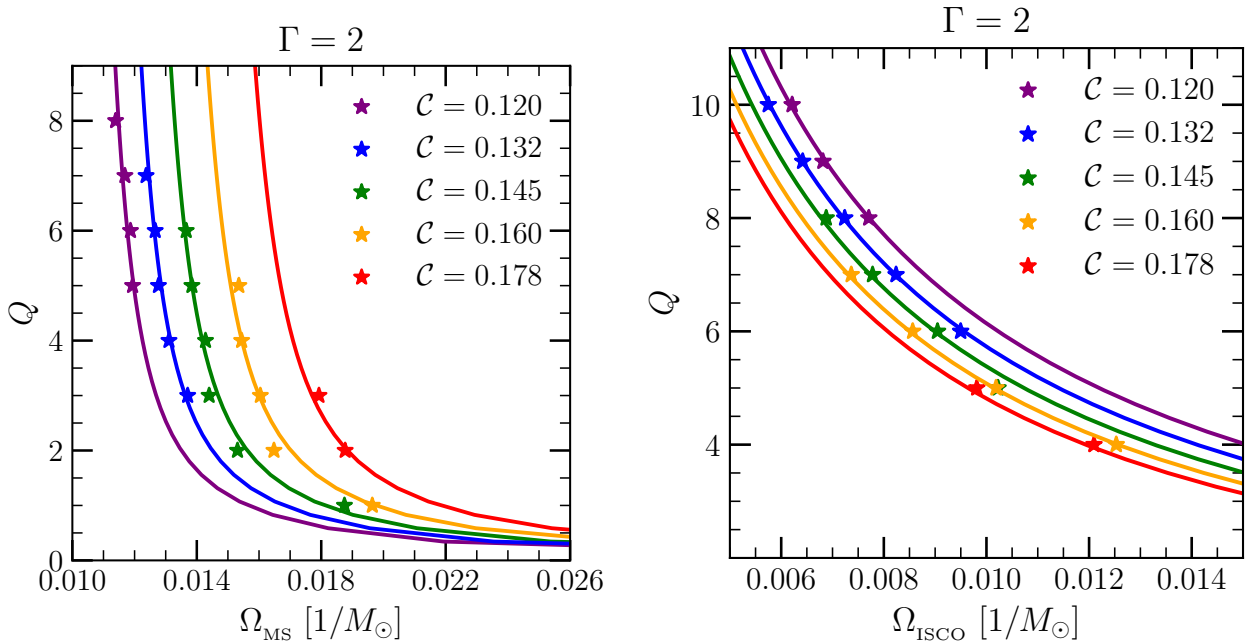


FIG. 6. *Left panel*: shown with coloured symbols are the extrapolated values of the orbital angular velocity at the onset of mass shedding along BHNS sequences of constant compactness  $\mathcal{C}$ . Solid lines of the same colour report the fit with the functional form given by Eq. (29). *Right panel*: the same as on the left but for the orbital angular velocity at the ISCO; also in this case, the solid lines show the fit given by Eq. (30).

EOS	$c_1$	$c_2$	$c_3$	$d_1$	$d_2$	$d_3$
$\Gamma = 2$	0.334	-0.218	-0.003	0.575	0.447	0.676
soft	0.221	2.994	-0.005	0.045	-1.078	2.055
intermediate	0.261	1.912	-0.010	0.126	-0.277	1.151
stiff	0.264	1.821	-0.011	0.049	-0.538	0.720

TABLE II. Best-fit parameters for the mass-shedding frequency  $\Omega_{\text{MS}}$  [see Eq. (29)] and ISCO frequency  $\Omega_{\text{ISCO}}$  [see Eq. (30)], for BHNS sequences employing either  $\Gamma = 2$  polytrope EOS or the three realistic EOSs considered here.

properly reproduce the relevant limits. For example, the compactness dependence in the functional form of  $\Omega_{\text{MS}}$  respects the limit  $\Omega_{\text{MS}} = 0$  for  $\mathcal{C} \rightarrow 0$ , since an infinitely extended NS is already “disrupted” at infinite separation. Similarly, the mass-ratio dependence in  $\Omega_{\text{ISCO}}$  is such that for the test particle limit  $1/Q \rightarrow 0$ ,  $M_{\text{tot}}\Omega_{\text{ISCO}} = 6^{-3/2}$ . In Table II we list the best-fit coefficients for the  $\Gamma = 2$  sequences that have been used to generate the solid lines in Fig. 6.

We note that while our functional modelling of  $\Omega_{\text{ISCO}}(Q, \mathcal{C})$  is different from that suggested in Ref. [40]<sup>6</sup>, it yields a match to the data that is quantitatively comparable. On the other hand, the modelling of  $\Omega_{\text{MS}}(Q, \mathcal{C})$  not only is functionally

different, but it also leads to a different description of our data, which is not well described by the fitting expressions suggested in Ref. [40]. More specifically, we find that the additional terms in  $q$  and  $\mathcal{C}$  are important to capture the behaviour of our QE sequences and that ignoring them leads to a systematic bias in the estimate of the mass-shedding limit ( $c_2 = c_3 = 0$  in Ref. [40]). In Fig. 6 we present the numerical data (coloured stars) and functional forms (30), (29) (coloured solid lines) along sequences of constant compactness for BHNS binaries where the NS is modelled with a  $\Gamma = 2$  EOS. Note how the fitting expressions reproduce the data very accurately despite the very steep changes in  $\Omega_{\text{MS}}$  and  $\Omega_{\text{ISCO}}$  with the mass ratio.

Finally, since we have expressions for  $\Omega_{\text{MS}}(Q, \mathcal{C})$  and  $\Omega_{\text{ISCO}}(Q, \mathcal{C})$ , it is interesting to mark in the  $(Q, \mathcal{C})$  space the set of points for which  $\Omega_{\text{MS}}(Q, \mathcal{C}) = \Omega_{\text{ISCO}}(Q, \mathcal{C})$ . This is shown in Fig. 7 for irrotational binaries ( $\chi_{\text{BH}} = 0$ ), where we report with a black solid line the condition for which the mass-shedding and the ISCO frequencies are the same. This separatrix essentially splits the space of parameters  $(Q, \mathcal{C})$  into two distinct regions. In the first one, indicated as “mass shedding” and shown with a green-shading,  $\Omega_{\text{MS}} < \Omega_{\text{ISCO}}$  and, hence, binaries here are characterised by the tidal disruption of the NS, such that a remnant disc can be produced and a potential electromagnetic counterpart is expected. In the second region, indicated as “plunge” and shown with a salmon-shading,  $\Omega_{\text{MS}} > \Omega_{\text{ISCO}}$ , implying that binaries in this region are characterised by the NS being absorbed by the BH essentially intact, such that no electromagnetic counterpart is to be expected.

Overall, the diagram shown in Fig. 7 shows rather clearly that mass-shedding for BHNS binaries with nonrotating BHs requires NSs that are not very compact (i.e., overall stiff

<sup>6</sup> In particular, Ref. [40] considers the ansatz  $M_{\text{tot}}\Omega_{\text{ISCO}} = c_1[1 - c_2q^{\lambda_1}(1 - c_3\mathcal{C}^{\lambda_2})]$  and first fixes the coefficients ( $c_1, c_2, c_3$ ) by requiring compatibility with the test-particle limit, an equal-mass BBH system and one representative BHNS binary, and subsequently chooses the powers of  $\lambda_{1,2}$  empirically to correspond well to the data. In contrast, our fitting function (30) respects by design only the test-particle limit and constrains the free coefficients entirely from the data.



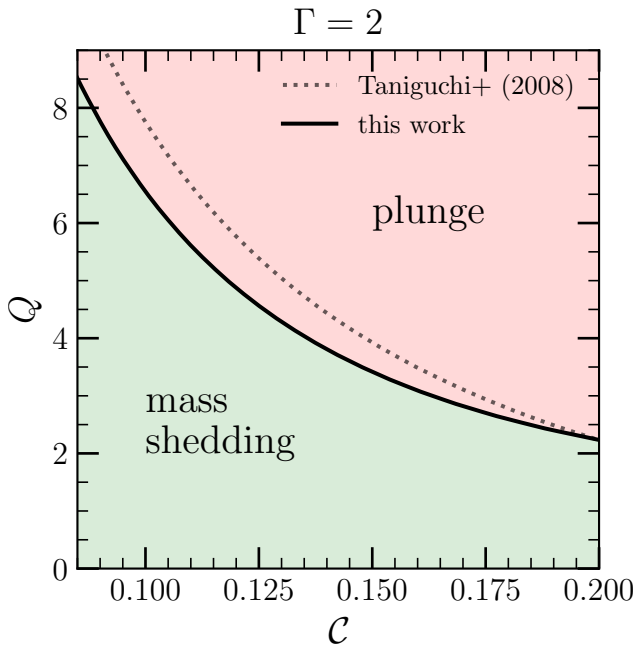


FIG. 7. Shown with a solid black line is the separatrix  $\Omega_{\text{MS}}(Q, \mathcal{C}) = \Omega_{\text{ISCO}}(Q, \mathcal{C})$  in the  $(Q, \mathcal{C})$  variables distinguishing between BHNS binaries leading to a “plunge” (salmon-shaded area) and to a disruption (green-shaded area). The data refers to the sequences with a  $\Gamma = 2$  polytrope reported in Fig. 6. Shown with a dotted line is the corresponding separatrix suggested in Ref. [40].

EOSs) for realistic mass ratios (i.e.,  $Q \gtrsim 5$ ). Alternatively, a plunge can still take place with smaller mass asymmetries (i.e.,  $Q \sim 2$ ), but requires very compact NSs (i.e., overall soft EOSs). We will see that this behaviour continues to apply when considering realistic EOSs (see Fig. 9). Finally, shown with a black dotted line in Fig. 7 is the representation of the separatrix as predicted in Ref. [40] and that, for the same compactness, predicts mass shedding for larger mass asymmetries or, alternatively, for larger compactness when holding the mass ratio constant. The difference between the two results is small and its origin is to be found in the different functional forms for  $\Omega_{\text{MS}}$  and  $\Omega_{\text{ISCO}}$ , which, as discussed above, leads to a systematic difference for binaries with small compactness.

### C. Realistic EOSs: irrotational sequences

We now turn our attention to sequences of BHNS initial data with three realistic EOSs of varying stiffness. Instead of considering QE sequences with constant rest-masses as was done for the polytropic EOS, we concentrate here on astrophysically relevant values of the gravitational mass, i.e.,  $M_{\text{NS}} = 1.2, 1.4, 1.8 M_{\odot}$ . Furthermore, because we consider three realistic EOSs with different stiffness, the corresponding ranges in compactness are not the same but overlap in the most astrophysically relevant regime  $\mathcal{C} = 0.15 - 0.2$ . Finally, we restrict the range of mass ratios to  $Q = 2 - 7$ , as realistic EOSs display greater compactnesses than the  $\Gamma = 2$

polytrope (see Fig. 3 and Tab. I).

For brevity, we do not report here the details of the behaviour of  $\kappa$  and  $E_{\text{b}}$  for sequences of constant mass ratio and NS gravitational mass, which are actually very similar to Fig. 6. Rather, we concentrate directly on the actual dependencies of  $\Omega_{\text{MS}}$  and  $\Omega_{\text{ISCO}}$  on  $Q$  and  $\mathcal{C}$  for the realistic EOSs. These are reported in Fig. 8, along with the result of the fit for the intermediate-stiffness EOS (analogous figures for the soft and stiff EOS are reported in Appendix C), where the best-fit parameters for  $\Omega_{\text{MS}}$  and  $\Omega_{\text{ISCO}}$  for each realistic EOS are listed in Tab. II.

When comparing Fig. 8 with the corresponding figure for polytropes (Fig. 6) it is easy to notice that, in particular for  $\Omega_{\text{MS}}$ , a significant difference appears in the sequence for  $M_{\text{NS}} = 1.8 M_{\odot}$  when compared to the other sequences at masses  $M_{\text{NS}} = 1.2, 1.4 M_{\odot}$ . The reason behind this behaviour has to be found in the fact that stellar models with  $M_{\text{NS}} = 1.8 M_{\odot}$  have a significantly larger compactness than those with  $M_{\text{NS}} = 1.4 M_{\odot}$  and this increases nonlinearly the values of  $\Omega_{\text{MS}}$ . Obviously, this behaviour is further amplified when comparing with the sequences of the  $\Gamma = 2$  polytropes and indeed, the compactness for the  $1.8 M_{\odot}$  NSs with the intermediate-stiffness EOS is  $\mathcal{C} = 0.214$  whereas the polytropic sequences reach  $\mathcal{C} = 0.1780$  at most<sup>7</sup>. For this reason we have introduced the parameter  $c_2$  specifically to capture the steeper dependence on the compactness.

In analogy with the analysis illustrated in Fig. 7, we report in Fig. 9 the separatrix curves for  $\Omega_{\text{MS}} = \Omega_{\text{ISCO}}$  relative to the three different realistic EOSs considered here and indicated with lines of different colours: green for the stiff EOS, red for the intermediate EOS and blue for the soft EOS. Unsurprisingly, the separatrices move systematically to larger frequencies for softer EOSs (see e.g., Fig. 16) and hence more compact NSs. The variance, however, is rather small especially when compared with what was observed for the simpler polytropes. Note also that the separatrices are very similar in the range of compactnesses  $0.14 \lesssim \mathcal{C} \lesssim 0.18$ . This “quasi-universal” behaviour will be exploited in Sec. IV D to deduce some EOS-independent considerations on the possibility of producing a massive merger remnant.

Also shown in Fig. 7 with a black dashed line is the separatrix as computed for  $\chi_{\text{BH}} = 0$  using the estimate for the remnant baryon mass of Foucart et al. [27]. More specifically, the separatrix in this case is given by the set of points in the  $(Q, \mathcal{C})$  plane for which the reduced remnant mass  $\hat{M}_{\text{rem}} = 10^{-2}$  [see Eq. (4) of Ref. [27]]<sup>8</sup>. Considering that the remnant-mass measurement of Ref. [27] combines a heterogeneous set of numerical-relativity simulations with different EOSs, mass ratios, and BH spins, the fact that its behaviour matches so well

<sup>7</sup> More precisely, the polytropic sequence reaches  $\mathcal{C} = 0.178$  for a  $1.56 M_{\odot}$  NS, which is already close to the TOV mass of  $1.62 M_{\odot}$  for that equation of state.

<sup>8</sup> A residual mass of  $\hat{M}_{\text{rem}} = 10^{-2}$  is here selected because the numerical solution of a BHNS binary with a DD2 EOS placed on the intermediate-stiffness separatrix would lead to a remnant disc with a mass of about  $10^{-2} M_{\odot}$  (see paper II [57]).

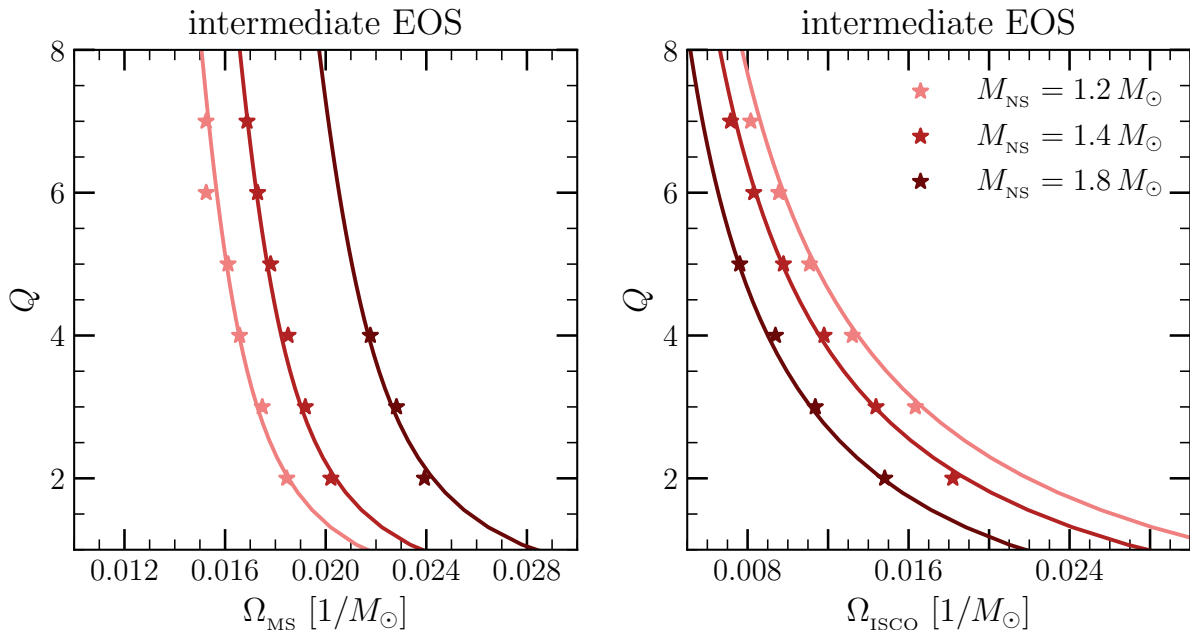


FIG. 8. The same as in Fig. 6 (i.e., mass-shedding frequencies on the left and ISCO frequencies on the right), but for the realistic EOS with intermediate stiffness and for BHNS sequences of constant NS mass, i.e.,  $M_{\text{NS}} = 1.2, 1.4, 1.8 M_{\odot}$ .

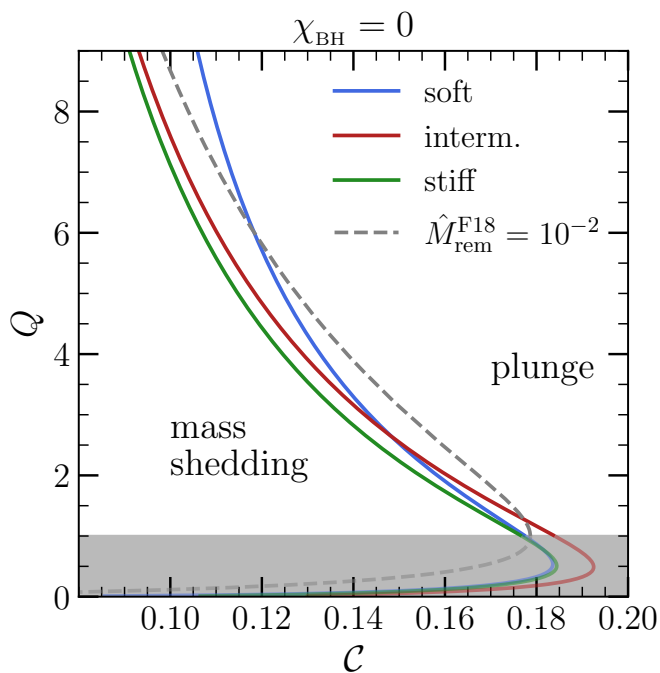


FIG. 9. The same as in Fig. 7, namely, the separatrix curves between plunge and disruption configurations, but for the three realistic EOSs considered here: soft (blue solid line), intermediate (red solid line), and stiff (green solid line). The BHNS binaries are irrotational (i.e.,  $\chi_{\text{BH}} = 0$ ) and the dashed gray line marks BHNS binaries with a normalized remnant mass  $\hat{M}_{\text{rem}} \geq 10^{-2}$  as estimated from the fitting model of Ref. [27]. A shaded region with semi-transparent curves shows the very different behaviour of the separatrices for mass ratios  $Q \leq 1$ .

	$e_1$	$e_2$	$e_3$
$g_{\text{MS}}$	0.008	-0.015	0.010
$g_{\text{ISCO}}$	0.819	0.455	--

TABLE III. Fitting parameters for functions modelling the spin dependence defined in Eq. (33) and Eq. (34), using the data presented in Fig. 10 and Fig. 17.

to the predictions obtained from QE sequences – which cannot account for nonlinear dynamical effects emerging during the inspiral and disruption – is overall very reassuring. As we will discuss below, the predictions for the separatrices shown in Fig. 9 will be further refined when considering the contributions to  $\Omega_{\text{ISCO}}$  and  $\Omega_{\text{MS}}$  coming from the BH spin (see Fig. 12).

Lastly, we note that all the separatrices in Fig. 9 show that their slopes change sign for very small mass ratios; this behaviour, which was absent in the case of the  $\Gamma = 2$  polytrope, happens around  $Q \approx 0.5$  for all the three EOSs considered in our study, and for  $Q \approx 1$  in the remnant-mass model of Ref. [27] (see grey-shaded area). Overall, this scenario, which is not expected to take place under realistic astrophysical conditions, highlights that for each EOS there exists a maximum compactness above which a NS cannot be disrupted outside the ISCO, no matter how small the BH mass is.

#### D. Realistic EOSs: binaries with a spinning BH

The results presented in this section follow the same methodology of the previous sections, but specifically concentrate on QE sequences of BHNS binaries where the BH

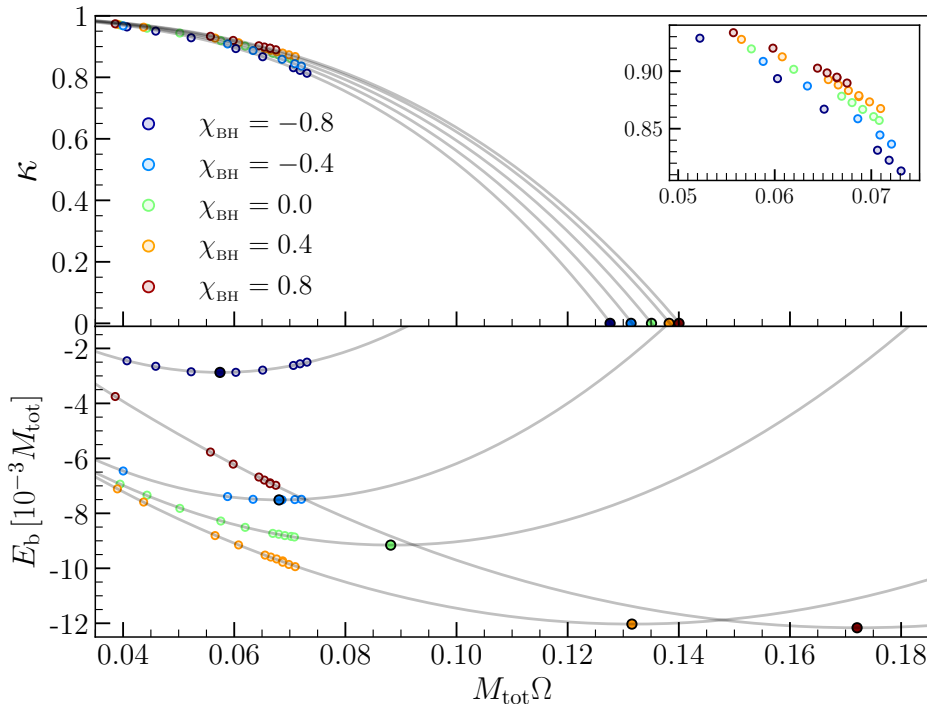


FIG. 10. The same as in Fig. 5, but for QE sequences with BHs having spins  $\chi_{\text{BH}} \in \{-0.8, -0.4, 0, 0.4, 0.8\}$ . The binaries have total masses  $M_{\text{tot}} = 7.8 M_{\odot}$ , a mass ratio  $Q = 5$  and employ the EOS with intermediate stiffness. Gray solid curves indicate the fitting functions and corresponding extrapolations mark the mass-shedding  $\Omega_{\text{MS}}$  and ISCO frequencies  $\Omega_{\text{ISCO}}$ ; the inset in the top panel highlights the behaviour of the numerical data.

is rotating with a different spin and is either aligned or anti-aligned with the orbital angular momentum. Obviously, this choice now increases the possible space of parameters, which is now given by  $(Q, \mathcal{C}, \chi_{\text{BH}})$ , making the problem harder to tackle in general terms. For this reason, and to keep the problem tractable, we restrict the EOS to be the one of intermediate stiffness and the ADM mass of the NS to be  $M_{\text{NS}} = 1.300 M_{\odot}$ , so that the corresponding baryon rest-mass and compactness is  $M_{\text{b}} = 1.423 M_{\odot}$  and  $\mathcal{C} = 0.168$ , respectively (see Fig. 9). In practice, this restriction actually focuses on what is potentially the most interesting region for realistic mass ratios  $Q \approx 5$ , as it leads to binaries whose merger outcome is most affected by the presence of a spinning BH. As a result, having fixed the EOS and the compactness, the problem becomes much more affordable in terms of computational costs and hence we explore 15 QE sequences of mass ratio  $Q = \{4, 5, 6\}$  and black-hole spin  $\chi_{\text{BH}} = \{-0.8, -0.4, 0.0, 0.4, 0.8\}$ .

Figure 10 provides a synthetic representation of QE sequences with fixed values of the BH spin and  $Q = 5$  in terms of the mass-shedding diagnostic  $\kappa$  (top panel) and the normalised binding energy (bottom panel). Also reported with gray solid lines are the functional fitting functions (25) and (27) so that it is easy to appreciate the corresponding values of  $\Omega_{\text{MS}}$  (i.e.,  $\kappa \rightarrow 0$  in the top panel) and of  $\Omega_{\text{ISCO}}$  (i.e.,  $\partial E_{\text{b}}/\partial\Omega = 0$  in the bottom panel). For compactness, equivalent figures for mass ratios  $Q = 4, 6$  are presented in Fig. 17 in Appendix C, while the numerical values relative to the  $Q = 5$  sequence are reported in Tab. IV for reproducibil-

ity.

The spin dependence present in Fig. 10 is clearly visible both in the mass-shedding indicator, as well as in the binding energy. From the values of  $\Omega_{\text{MS}}$  and  $\Omega_{\text{ISCO}}$  it is apparent that both diagnostics capture the dependence on the BH spin in a manner that is consistent with the predictions of tidal forces in Kerr spacetime [86, 91] (see also our discussion of the tidal forces in Sec. III C) and the analytical dependence of the ISCO location for massive test particles in the Kerr solution. More specifically, we find that anti-aligned BH spins decrease systematically the values of  $\kappa$  and hence yield smaller values of  $\Omega_{\text{MS}}$ . Similarly, the BH spin affects the slope of the  $E_{\text{b}}-\Omega$  curves to such extent that for anti-aligned spins we can measure  $\Omega_{\text{ISCO}}$  already among the initial data configurations without having to resort to an extrapolation. Interestingly, a similar behaviour has been reported also for BH binaries with anti-aligned spins [66]. On the other hand, BHs with aligned spins tend to increase the (absolute value of the) slope of the  $E_{\text{b}}-\Omega$  curves and thus move the minima towards higher orbital angular velocities. Again, this is exactly the expectation from the dependence of ISCO for test-particles, for which positive (prograde) spins tend to push the radius of the ISCO inwards, i.e., to higher orbital frequencies.

At this point, using the information from the 15 QE sequences computed, we can express analytically and for the first time the impact the BH spin has on the mass-shedding and ISCO frequencies. Stated differently, we can use the bulk of data computed to derive extensions of expressions (29) and

(30) to include also a dependence on  $\chi_{\text{BH}}$ .

An effective and accurate manner to include this additional dependence is to assume that it can be expressed as a correction to the zero-spin expressions and hence we assume that the general expressions of  $\Omega_{\text{MS, ISCO}} = \Omega_{\text{MS, ISCO}}(Q, \mathcal{C}, \chi_{\text{BH}})$  have the form

$$\Omega_{\text{MS}}(Q, \mathcal{C}, \chi_{\text{BH}}) := \Omega_{\text{MS}}(Q, \mathcal{C}) g_{\text{MS}}(Q, \chi_{\text{BH}}), \quad (31)$$

$$\Omega_{\text{ISCO}}(Q, \mathcal{C}, \chi_{\text{BH}}) := \Omega_{\text{ISCO}}(Q, \mathcal{C}) g_{\text{ISCO}}(\chi_{\text{BH}}), \quad (32)$$

where the  $\Omega_{\text{MS, ISCO}}(Q, \mathcal{C})$  are the zero-spin results given by expressions (29) and (30) and discussed in Sec. IV C. On the other hand,  $g_{\text{MS}}(Q, \chi_{\text{BH}})$  and  $g_{\text{ISCO}}(\chi_{\text{BH}})$  are to be seen as the additional spin-induced corrections to the relevant frequencies. Note that in the case of the mass-shedding frequency, the data reveals that the spin-induced corrections also depend on the mass ratio and hence we need to express this via a function  $g_{\text{MS}} = g_{\text{MS}}(Q, \chi_{\text{BH}})$ ; such a dependence is absent for the ISCO frequency, so that  $g_{\text{ISCO}} = g_{\text{ISCO}}(\chi_{\text{BH}})$  (see also the right panel of Fig. 11). At the same time, we adopt the same spin dependence for  $g_{\text{MS}}$  and  $g_{\text{ISCO}}$ , whose full expressions are then given by

$$g_{\text{MS}}(Q, \chi_{\text{BH}}) := (1 + e_1 \chi_{\text{BH}} + e_2 \chi_{\text{BH}}^2) (1 + e_3 \chi_{\text{BH}} Q), \quad (33)$$

$$g_{\text{ISCO}}(\chi_{\text{BH}}) := (1 + e_1 \chi_{\text{BH}} + e_2 \chi_{\text{BH}}^2), \quad (34)$$

where  $(e_1, e_2, e_3)$  are free parameters to be computed by the fit and where the functional dependence guarantees the correct zero-spin limits, i.e.,  $g_{\text{MS}}(Q, 0) = 1$  and  $g_{\text{ISCO}}(0) = 1$ .

Figure 11 reports the dependence on the BH spin of the mass-shedding frequency (left panel) and of the ISCO frequency (right panel) when rescaled by their corresponding zero-spin values, i.e.,  $\Omega_{\text{MS, ISCO}}/\Omega_{\text{MS, ISCO}}^{\chi_{\text{BH}}=0}$ , so as to best appreciate the differences and provide justification for the chosen modelling functions (33) and (34). More specifically, reported with different symbols are the data points along the various constant mass-ratio sequences while the dashed black lines are computed from the fitting functions given by Eqs. (33) (left panel) and (34) (right panel), respectively. The numerical values of the best-fit coefficients ( $e_i$ ) are reported in Tab. III. Note that the change in the  $\Omega_{\text{MS}}$  due to the spin is rather small and at most around  $\approx 6\%$ , with a slight residual dependence on the mass ratio. On the contrary, the BH spin significantly impacts  $\Omega_{\text{ISCO}}$ , with  $\Omega_{\text{ISCO}}^{\chi_{\text{BH}}=-0.8} \approx 0.6 \Omega_{\text{ISCO}}^{\chi_{\text{BH}}=0}$  and  $\Omega_{\text{ISCO}}^{\chi_{\text{BH}}=0.8} \approx 2.1 \Omega_{\text{ISCO}}^{\chi_{\text{BH}}=0}$ . Interestingly, it is possible to compare the behaviour of the ISCO frequency to the case of a test-particle in a Kerr-BH spacetime. This is shown as a gray dashed line in Fig. 11 and it is quite remarkable that the test-particle behaviour is very similar to the one we have measured in our BHNS binaries in the case of anti-aligned spins<sup>9</sup>. On

the other hand, significant differences appear in the case of aligned spins, where the results of the QE sequences show a smaller increase with spin and where the test-particle jump is  $\Omega_{\text{ISCO}}^{\chi_{\text{BH}}=0.8} \approx 2.6 \Omega_{\text{ISCO}}^{\chi_{\text{BH}}=0}$ . The origin of this behaviour is to be found in the fact that the location of the ISCO moves out to larger distances in the case of anti-aligned spins, hence in regions of the spacetime where the curvature is smaller and the point-particle approximation is more accurate. On the other hand, the location of the ISCO moves in for aligned spins, where strong-curvature and finite-size effects of the NS are responsible for the differences seen in Fig. 11. Overall, these considerations clearly highlight that the role of the BH spin is essential in determining the location of the ISCO and hence the merger outcome. On the other hand, the BH spin plays only a minor role in determining the mass-shedding location.

### E. $\Omega_{\text{MS}}$ and $\Omega_{\text{ISCO}}$ : dependence on $q, \mathcal{C}$ , and $\chi_{\text{BH}}$

Having defined via expressions (31) – (34) the functional dependencies of the mass-shedding and ISCO frequencies, we can now assess the separatrix of the “mass-shedding” and “plunge” configurations in the three-dimensional space of parameters  $(Q, \mathcal{C}, \chi_{\text{BH}})$ . As done in .. 7 and 9, we determine this separatrix by requiring that  $\Omega_{\text{MS}} = \Omega_{\text{ISCO}}$ . The resulting surface is shown in Fig. 12 and deserves a number of remarks. First, we recall that while this separatrix is obtained for the intermediate-stiffness EOS, we expect the functional behaviour to be the same also for different EOSs. Second, it demonstrates that for a fixed stellar compactness aligned BH spins are able to disrupt the NS at systematically larger mass asymmetries so that, for instance, a reference value of  $\mathcal{C} = 0.15$  will lead to disruption at  $\chi_{\text{BH}} = 0.8$  for  $Q = 7$ , while this can be achieved for at most  $Q \approx 2.6$  for  $\chi_{\text{BH}} = 0.0$ . Similarly, for a fixed mass asymmetry, large aligned BH spins can result in a NS disruption with systematically more compact stars so that, for instance, a reference value of  $Q = 5$  will lead to disruption at  $\chi_{\text{BH}} = 0.8$  for  $\mathcal{C} = 0.1718$ , while this can only be achieved at compactnesses  $\mathcal{C} \approx 0.12$  for  $\chi_{\text{BH}} = 0.0$ .

Because the critical separatrix given by the function  $Q_{\text{crit}}(\mathcal{C}, \chi_{\text{BH}})$  is defined only implicitly through the condition  $\Omega_{\text{MS}} = \Omega_{\text{ISCO}}$ , an explicit analytic expression in terms of elementary functions, or possibly even a single-branch solution in terms of special functions, is unlikely to exist (non-integer powers of  $q$  and  $\mathcal{C}$  are employed in the fitting functions (33) and (34)). However, we can parametrize the surface in terms of a simple fitting function  $Q_{\text{fit}}$  given by the multiplication of two cubic polynomials in  $\chi_{\text{BH}}$  and  $\mathcal{C}$

$$Q_{\text{fit}} = p_0(1 + k_1 \chi_{\text{BH}} + k_2 \chi_{\text{BH}}^2 + k_3 \chi_{\text{BH}}^3) \quad (35)$$

$$(1 + \ell_1 \mathcal{C} + \ell_2 \mathcal{C}^2 + \ell_3 \mathcal{C}^3). \quad (36)$$

The above function provides a very good approximation of the separatrix surface reported in Fig. 12 and the corresponding best-fit results are given respectively by  $p_0 = 24.484$ ,  $k_1 = 1.464$ ,  $k_2 = 0.963$ ,  $k_3 = -0.162$ ,  $\ell_1 = -11.863$ ,  $\ell_2 = 50.877$ , and  $\ell_3 = -77.050$ . The analytic representation of the critical surface provides a rather accurate description of the numerical data with a coefficient of determination

<sup>9</sup> Note that the normalization factor in the ISCO frequencies, i.e.,  $\Omega_{\text{ISCO}}^{\chi_{\text{BH}}=0}$  is different whether one is considering BHNS binaries or a test particle. However, once the scaling is done, the functional behaviour of  $\Omega_{\text{ISCO}}/\Omega_{\text{ISCO}}^{\chi_{\text{BH}}=0}$  is the same for anti-aligned spins, as shown in Fig. 11.



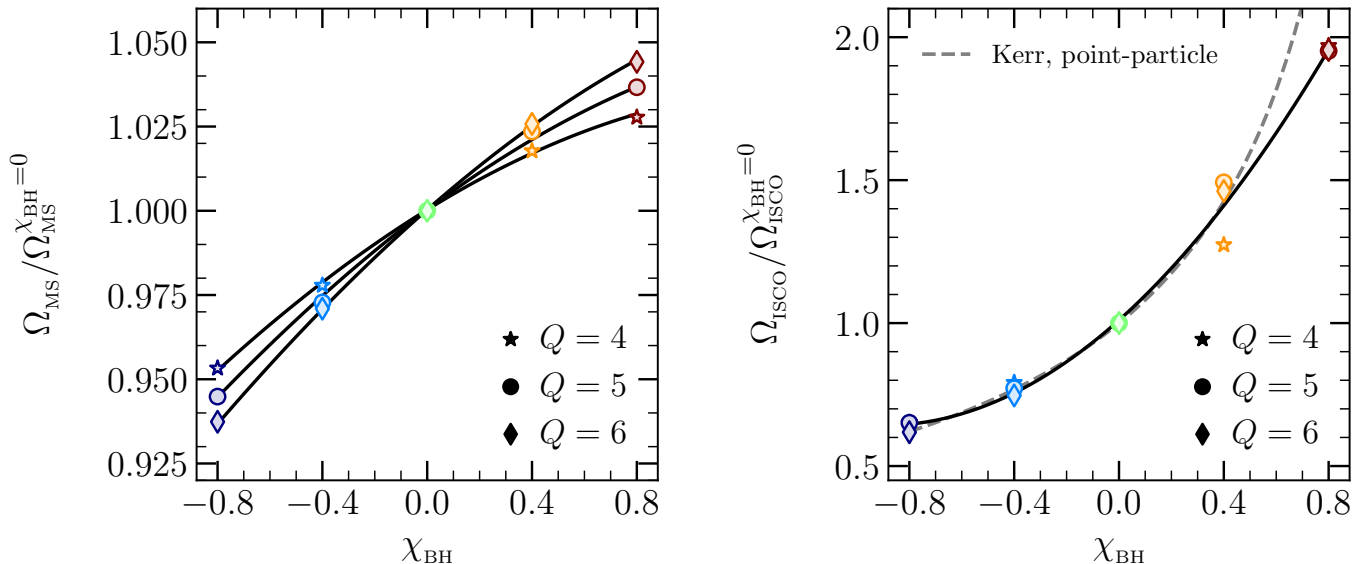


FIG. 11. Orbital angular velocity at mass-shedding  $\Omega_{\text{MS}}$  (left panel) and at the ISCO  $\Omega_{\text{ISCO}}$  (right panel) when rescaled by the corresponding values for irrotational BHNS binaries  $\Omega_{\text{MS,ISCO}}^{\chi_{\text{BH}}=0}$  so as to remove the mass-ratio and compactness dependence. The data is presented with symbols of different type along sequences of mass ratio  $Q \in \{4, 5, 6\}$ . Shown with black solid lines are the results of the fits using expressions (33) and (34) for the various sequences of varying mass ratio. Shown with a gray dashed line on the right panel is the corresponding behaviour of  $\Omega_{\text{ISCO}}/\Omega_{\text{ISCO}}^{\chi_{\text{BH}}=0}$  for a test particle around a Kerr BH, highlighting that deviations appear mostly for aligned and rapidly rotating BHs.

$R^2 = 0.988$ , and relative differences that are smaller than 6.2% for binaries with  $Q \geq 1$ .

Although Fig. 12 provides a complete and comprehensive representation of the QE sequences, a different and possibly more useful representation is also possible. In particular, recalling that the behaviour of the separatrix between the mass-shedding and plunge solutions is not very sensitive to the EOS and hence “quasi-universal” in the range of compactnesses  $0.14 \lesssim \mathcal{C} \lesssim 0.18$  (see Fig. 9 and discussion in Sec. IV C), we can consider a NS with a given mass  $M_{\text{NS}}$  and map the dependence on the compactness into a dependence on the stellar radius defined as  $R_{\text{NS}} = M_{\text{NS}}/\mathcal{C}$ . This is what is shown in Fig. 13, which reports the mass ratio as a function of stellar radius and BH spin along the separatrix surface  $\Omega_{\text{MS}} = \Omega_{\text{ISCO}}$  and for a fixed NS mass of  $M_{\text{NS}} = 1.35 M_{\odot}$ . With this representation, and after fixing a critical mass ratio  $Q_{\text{crit}}$ , it is simple to appreciate the radius above which the star will be tidally disrupted. Furthermore, this mapping facilitates the comparison with the similar Fig. 2 in Ref. [92], which is built considering a separatrix yielding the zero value for the remnant mass  $\hat{M}_{\text{rem}}$ . To facilitate the comparison between the two approaches, and in light of our finding in Fig. 9, we report with gray dashed lines in Fig. 13 the corresponding  $Q_{\text{crit}}$  contours obtained in terms of the remnant mass  $\hat{M}_{\text{rem}} = 10^{-2}$ . Overall, the contour lines are very similar despite the systematic differences in the way they are computed (quasi-stationary sequences or collection of dynamical simulations) and highlight that a reference NS with a mass of  $1.35 M_{\odot}$  with a representative radius of  $\simeq 12.5 \text{ km}$  [76] and a mass ratio  $Q_{\text{crit}} = 3$  would only be disrupted before merger by a BH with spin  $\chi_{\text{BH}} \gtrsim 0.4$ ; conversely, the same star in a binary with mass ratio of  $Q_{\text{crit}} = 5$  would then require the BH to have a larger

spin of  $\chi_{\text{BH}} \gtrsim 0.8$ . Furthermore, in the case of a GW230529-like event with  $Q \sim 2.56$  [2], the minimum BH spin would need to be  $\chi_{\text{BH}} \gtrsim 0$  for tidal disruption to occur.

## V. CONCLUSIONS

In this first paper in a series about the equilibrium and dynamical properties of BHNS binaries, we have investigated QE sequences of BHNS initial data employing an improved version of the initial-data solver FUKA, thus making use of what is arguably the largest collection of individual BHNS configurations reported in the literature. In addition, besides considering standard quantities for monitoring the occurrence of mass-shedding or the occurrence of an unstable circular orbit, we have also presented a novel approach based on the study of tidal forces in terms of projections of the curvature tensor in a suitable frame that provides a considerable amount of insight on the forces and deformations taking place within the NS matter.

More specifically, we have first reported an extensive testing of the new code by comparing its solutions for a  $\Gamma = 2$  polytropic EOS and finding very good agreement with the results published in Ref. [40]. Having established the ability of the new code to produce accurate initial data of BHNS binaries, we have used it to investigate QE sequences of irrotational binaries, i.e., where the BH is nonrotating, under a variety of mass ratios and employing three distinct EOSs extracted from an ensemble generated by uniform sampling with the speed-of-sound parametrization and selected so as to provide a spread in the EOS stiffness. In this way, we were able to determine and express analytically not only the mass-

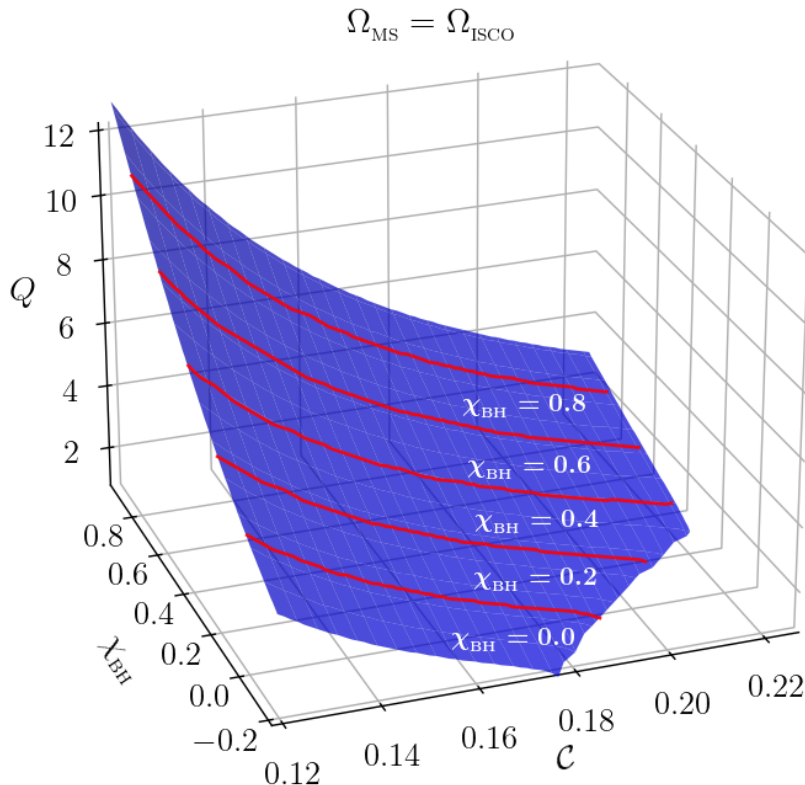


FIG. 12. Shown in blue is the separatrix surface between plunge and disruption configurations as obtained implicitly by the condition  $\Omega_{\text{MS}} = \Omega_{\text{ISCO}}$ . Such surface represents the extension of the separatrix curves shown in Fig. 9 and hence splits the space of parameters into regions leading to tidal disruption or plunge of the NS. The data refers to BHNS binaries with the intermediate-stiffness EOS and contours of constant BH spin are shown with red solid lines. Expression (35) provides a good fit of the functional dependence to the data on the blue surface.

shedding frequency as a function of the mass ratio and stellar compactness  $\Omega_{\text{MS}}(Q, \mathcal{C})$ , but also the related ISCO frequency  $\Omega_{\text{ISCO}}(Q, \mathcal{C})$ .

The ability to express analytically  $\Omega_{\text{MS}}$  and  $\Omega_{\text{ISCO}}$  has further allowed us to determine in the  $(Q, \mathcal{C})$  space the location of the separatrix for which  $\Omega_{\text{MS}} = \Omega_{\text{ISCO}}$  and thus to determine which combinations of mass ratios and compactnesses in the BHNS binary lead to either a “mass-shedding” scenario (i.e., the tidal disruption of the NS and the production of a massive merger remnant) or a “plunge” (i.e., the accretion of the NS without disruption). Interestingly, in a small but nonzero range of compactnesses, i.e., for  $0.14 \lesssim \mathcal{C} \lesssim 0.18$ , the threshold between the two scenarios is only weakly dependent on the EOS. In turn, this allows to draw conclusions on the disruption scenario that can be expressed in terms of stellar radii.

The study of QE sequences of irrotational BHNS binaries has been further extended by considering binaries in which the BH is spinning at different rates and with spins that are either aligned or anti-aligned with the orbital angular momentum. However, to make this study tractable from a computational point of view, the investigation of spinning BHNS binaries has been restricted to a single realistic EOS, namely the one

with intermediate stiffness. Also in this case, by determining the mass-shedding and the ISCO frequencies and expressing them analytically in the three-dimensional space of parameters  $(Q, \mathcal{C}, \chi_{\text{BH}})$  it was possible to establish the location of the separatrix  $\Omega_{\text{MS}} = \Omega_{\text{ISCO}}$  and hence the combinations of mass ratio, compactness and BH spin that can lead to a tidal disruption and hence to a massive merger remnant. To the best of our knowledge, this is the first time that the dependence of these frequencies on the BH spin is investigated and that such a threshold surface has been presented. Finally, exploiting the fact that for  $0.14 \lesssim \mathcal{C} \lesssim 0.18$  the threshold between the two scenarios is essentially EOS independent, we have mapped the predictions about the disruption from the  $(Q, \mathcal{C}, \chi_{\text{BH}})$  space into a prediction in the  $(Q, R_{\text{NS}}, \chi_{\text{BH}})$  space for the reference case of a NS with a mass of  $1.35 M_{\odot}$ . In turn, this has revealed that, for instance, a reference value of  $\mathcal{C} = 0.15$  can lead to disruption at  $\chi_{\text{BH}} = 0.8$  for  $Q = 7$ , while only at most  $Q \approx 3$  is admissible for  $\chi_{\text{BH}} = 0.0$ .

The analysis performed here can be extended in several directions. First, our results could be compared with those obtained when abandoning the assumption of conformal flatness, i.e., where in the NS region, non-diagonal terms of the spatial metric are nonzero. Such a comparison would be especially

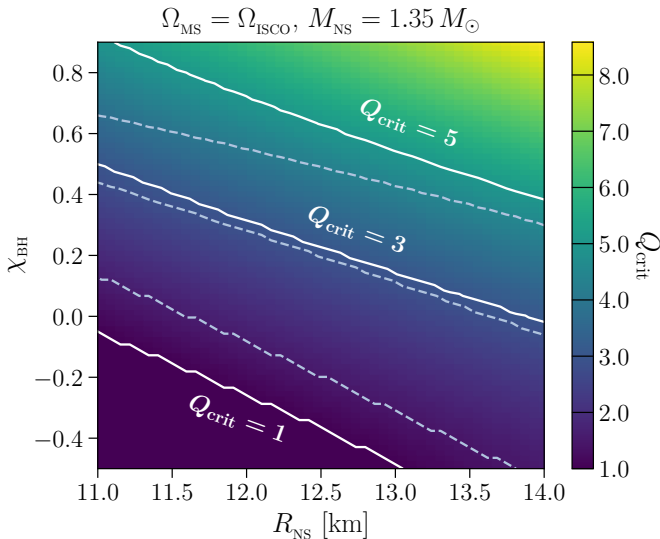


FIG. 13. Critical value of the mass ratio along the separatrix surface  $\Omega_{\text{MS}} = \Omega_{\text{ISCO}}$  shown as a function of the BH spin  $\chi_{\text{BH}}$  and NS radius for a fixed NS mass of  $1.35 M_{\odot}$ . The expressions used are Eq. (31) and Eq. (32) with best-fit parameters for the intermediate EOS. White solid lines show contours at fixed  $Q$ , while dashed lines report the corresponding contours when considering a normalized remnant mass  $\hat{M}_{\text{rem}} \geq 10^{-2}$  as estimated from the fitting model of Ref. [27].

useful to study the impact that conformal flatness has on the tidal-force analysis presented here and on the influence that BH spin exerts on the  $\kappa$  and  $E_b$  diagnostics. Unfortunately, we are not aware of initial-data solvers that can explore this avenue at present. Second, it would be interesting and actually important to consider additional EOSs to establish on more general grounds whether a quasi-universal behaviour is

present in the separatrix surface between a tidal disruption and a plunge scenario. Third, given that our QE sequences with an irrotational or aligned BH do not feature a minimum in the  $E_b$  curves, it would be interesting to explore other approaches that could potentially feature these minima, or be capable of approaching closer separations, thus yielding better estimates of the ISCO frequencies. Finally, a comparison could be carried out between the mass-shedding and ISCO frequency estimates made from our QE sequences and those instead inferred from fully dynamical general-relativistic hydrodynamic simulations. Such a comparison for a limited set of binaries will be presented in our accompanying paper II [57].

#### DATA AVAILABILITY

The QE sequences data can be shared after a reasonable request.

#### ACKNOWLEDGMENTS

We thank C. Ecker for sharing the ensemble of constraint-satisfying equations of state and their PDF that we used for this work, as well as for useful discussions and comments. KT expresses his gratitude to R. Duqué for extensive discussions on BHNS binaries. Support in funding comes from the State of Hesse within the Research Cluster ELEMENTS (Project ID 500/10.006), from the ERC Advanced Grant “JETSET: Launching, propagation and emission of relativistic jets from binary mergers and across mass scales” (Grant No. 884631). LR acknowledges the Walter Greiner Gesellschaft zur Förderung der physikalischen Grundlagenforschung e.V. through the Carl W. Fueck Laureatus Chair. The computations were performed on HPE Apollo HAWK at the High Performance Computing Center Stuttgart (HLRS) under the grants BNSMIC and BBHDISKS. ST gratefully acknowledges support from NASA award ATP-80NSSC22K1898.

- 
- [1] The LIGO Scientific Collaboration, the VIRGO Collaboration, and the KAGRA Collaboration, *Astrophys. J. Lett.* **915**, L5 (2021), [arXiv:2106.15163 \[astro-ph.HE\]](#).
  - [2] The LIGO Scientific Collaboration, the Virgo Collaboration, and the KAGRA Collaboration, [arXiv e-prints](#), [arXiv:2404.04248 \(2024\)](#), [arXiv:2404.04248 \[astro-ph.HE\]](#).
  - [3] B. P. Abbott *et al.* (LIGO Scientific, Virgo), *Phys. Rev. Lett.* **119**, 161101 (2017), [arXiv:1710.05832 \[gr-qc\]](#).
  - [4] A. Colombo *et al.*, [arXiv:2310.16894 \[astro-ph.HE\]](#) (2023).
  - [5] Z. B. Etienne, J. A. Faber, Y. T. Liu, S. L. Shapiro, K. Taniguchi, and T. W. Baumgarte, *Phys. Rev. D* **77**, 084002 (2008), [arXiv:0712.2460](#).
  - [6] M. Shibata and K. Taniguchi, *Phys. Rev. D* **77**, 084015 (2008), [arXiv:0711.1410](#).
  - [7] Z. B. Etienne, Y. T. Liu, S. L. Shapiro, and T. W. Baumgarte, *Phys. Rev. D* **79**, 044024 (2009), [arXiv:0812.2245 \[astro-ph\]](#).
  - [8] K. Kyutoku, M. Shibata, and K. Taniguchi, *Phys. Rev. D* **82**, 044049 (2010), [arXiv:1008.1460 \[astro-ph.HE\]](#).
  - [9] K. Kyutoku, H. Okawa, M. Shibata, and K. Taniguchi, *Phys. Rev. D* **84**, 064018 (2011), [arXiv:1108.1189 \[astro-ph\]](#).
  - [10] F. Foucart, M. D. Duez, L. E. Kidder, M. A. Scheel, B. Szilagy, and S. A. Teukolsky, *Phys. Rev. D* **85**, 044015 (2012), [arXiv:1111.1677 \[gr-qc\]](#).
  - [11] K. Kawaguchi, K. Kyutoku, H. Nakano, H. Okawa, M. Shibata, and K. Taniguchi, *Phys. Rev. D* **92**, 024014 (2015), [arXiv:1506.05473 \[astro-ph.HE\]](#).
  - [12] F. Foucart, M. D. Duez, L. E. Kidder, S. M. Nissanke, H. P. Pfeiffer, and M. A. Scheel, *Phys. Rev. D* **99**, 103025 (2019), [arXiv:1903.09166 \[astro-ph.HE\]](#).
  - [13] E. R. Most, L. J. Papenfort, S. D. Tootle, and L. Rezzolla, *Astrophys. J.* **912**, 80 (2021), [arXiv:2012.03896 \[astro-ph.HE\]](#).
  - [14] Z. B. Etienne, Y. T. Liu, V. Paschalidis, and S. L. Shapiro, *Phys. Rev. D* **85**, 064029 (2012), [arXiv:1112.0568 \[astro-ph.HE\]](#).
  - [15] K. Kyutoku, K. Kiuchi, Y. Sekiguchi, M. Shibata, and K. Taniguchi, *Phys. Rev. D* **97**, 023009 (2018), [arXiv:1710.00827 \[astro-ph.HE\]](#).
  - [16] K. Kyutoku, K. Ioka, and M. Shibata, *Phys. Rev. D* **88**, 041503 (2013), [arXiv:1305.6309 \[astro-ph.HE\]](#).
  - [17] C. Barbieri, O. S. Salafia, M. Colpi, G. Ghirlanda, A. Perego, and A. Colombo, *Astrophys. J.* **887**, L35 (2019),

- arXiv:1912.03894 [astro-ph.HE].
- [18] F. Pannarale, L. Rezzolla, F. Ohme, and J. S. Read, *Phys. Rev. D* **84**, 104017 (2011), arXiv:1103.3526 [astro-ph.HE].
- [19] B. D. Lackey, K. Kyutoku, M. Shibata, P. R. Brady, and J. L. Friedman, *Phys. Rev. D* **85**, 044061 (2012), arXiv:1109.3402 [astro-ph.HE].
- [20] B. D. Lackey, K. Kyutoku, M. Shibata, P. R. Brady, and J. L. Friedman, *Phys. Rev. D* **89**, 043009 (2014), arXiv:1303.6298 [gr-qc].
- [21] F. Pannarale, *Phys. Rev. D* **88**, 104025 (2013), arXiv:1208.5869 [gr-qc].
- [22] F. Pannarale, *Phys. Rev. D* **89**, 044045 (2014), arXiv:1311.5931 [gr-qc].
- [23] F. Zappa, S. Bernuzzi, F. Pannarale, M. Mapelli, and N. Giacobbo, *Phys. Rev. Lett.* **123**, 041102 (2019), arXiv:1903.11622 [gr-qc].
- [24] F. Pannarale, A. Tonita, and L. Rezzolla, *Astrophys. Journ.* **727**, 95 (2011), arXiv:1007.4160 [astro-ph.HE].
- [25] F. Foucart, *Phys. Rev. D* **86**, 124007 (2012), arXiv:1207.6304 [astro-ph.HE].
- [26] K. Kyutoku, K. Ioka, H. Okawa, M. Shibata, and K. Taniguchi, *Phys. Rev. D* **92**, 044028 (2015), arXiv:1502.05402 [astro-ph.HE].
- [27] F. Foucart, T. Hinderer, and S. Nisanke, *Phys. Rev. D* **98**, 081501 (2018), arXiv:1807.00011 [astro-ph.HE].
- [28] C. J. Krüger and F. Foucart, *Phys. Rev. D* **101**, 103002 (2020), arXiv:2002.07728 [astro-ph.HE].
- [29] L. Rezzolla, L. Baiotti, B. Giacomazzo, D. Link, and J. A. Font, *Class. Quantum Grav.* **27**, 114105 (2010), arXiv:1001.3074 [gr-qc].
- [30] V. Paschalidis, M. Ruiz, and S. L. Shapiro, *Astrophys. J. Lett.* **806**, L14 (2015), arXiv:1410.7392 [astro-ph.HE].
- [31] M. Ruiz, S. L. Shapiro, and A. Tsokaros, *Phys. Rev. D* **98**, 123017 (2018), arXiv:1810.08618 [astro-ph.HE].
- [32] E. R. Most, L. J. Papenfort, S. D. Tootle, and L. Rezzolla, *Monthly Notices of the Royal Astronomical Society* **506**, 3511 (2021), arXiv:2106.06391 [astro-ph.HE].
- [33] K. Hayashi, S. Fujibayashi, K. Kiuchi, K. Kyutoku, Y. Sekiguchi, and M. Shibata, *Phys. Rev. D* **106**, 023008 (2022).
- [34] O. Gottlieb *et al.*, *Astrophys. J. Lett.* **954**, L21 (2023), arXiv:2306.14947 [astro-ph.HE].
- [35] K. Hayashi, K. Kiuchi, K. Kyutoku, Y. Sekiguchi, and M. Shibata, *Phys. Rev. D* **107**, 123001 (2023).
- [36] R. D. Blandford and R. L. Znajek, *Mon. Not. R. Astron. Soc.* **179**, 433 (1977).
- [37] M. D. Duez, arXiv:2404.14782 [astro-ph.HE] (2024).
- [38] K. Taniguchi, T. W. Baumgarte, J. A. Faber, and S. L. Shapiro, *Phys. Rev. D* **74**, 041502 (2006), arXiv:gr-qc/0609053.
- [39] K. Taniguchi, T. W. Baumgarte, J. A. Faber, and S. L. Shapiro, *Phys. Rev. D* **75**, 084005 (2007).
- [40] K. Taniguchi, T. W. Baumgarte, J. A. Faber, and S. L. Shapiro, *Phys. Rev. D* **77**, 044003 (2008), arXiv:0710.5169 [gr-qc].
- [41] L. Rezzolla and O. Zanotti, *Relativistic Hydrodynamics* (Oxford University Press, Oxford, UK, 2013).
- [42] P. Grandclément, *Phys. Rev. D* **74**, 124002 (2006).
- [43] K. Kyutoku, M. Shibata, and K. Taniguchi, *Phys. Rev. D* **79**, 124018 (2009), arXiv:0906.0889 [gr-qc].
- [44] K. Henriksson, F. Foucart, L. E. Kidder, and S. A. Teukolsky, *Class. Quant. Grav.* **33**, 105009 (2016), arXiv:1409.7159 [gr-qc].
- [45] N. Tacik, F. Foucart, H. P. Pfeiffer, C. Muhlberger, L. E. Kidder, M. A. Scheel, and B. Szilágyi, *Class. Quant. Grav.* **33**, 225012 (2016), arXiv:1607.07962 [gr-qc].
- [46] A. Rashti, F. M. Fabbri, B. Brügmann, S. V. Chaurasia, T. Dietrich, M. Ujevic, and W. Tichy, *Phys. Rev. D* **105**, 104027 (2022), arXiv:2109.14511 [gr-qc].
- [47] L. J. Papenfort, S. D. Tootle, P. Grandclément, E. R. Most, and L. Rezzolla, *Phys. Rev. D* **104**, 024057 (2021).
- [48] e. a. Tootle, S., in preparation (2024), arXiv:in preparation.
- [49] S. D. Tootle, L. J. Papenfort, E. R. Most, and L. Rezzolla, *Astrophys. J. Lett.* **922**, L19 (2021), arXiv:2109.00940 [gr-qc].
- [50] L. J. Papenfort, E. R. Most, S. Tootle, and L. Rezzolla, *Mon. Not. Roy. Astron. Soc.* **513**, 3646 (2022), arXiv:2201.03632 [astro-ph.HE].
- [51] H.-J. Kuan, K. Van Aelst, A. T.-L. Lam, and M. Shibata, *Phys. Rev. D* **108**, 064057 (2023), arXiv:2309.01709 [gr-qc].
- [52] H.-J. Kuan, A. T.-L. Lam, D. D. Doneva, S. S. Yazadjiev, M. Shibata, and K. Kiuchi, *Phys. Rev. D* **108**, 063033 (2023), arXiv:2302.11596 [gr-qc].
- [53] I. Markin, A. Neuweiler, A. Abac, S. V. Chaurasia, M. Ujevic, M. Bulla, and T. Dietrich, *Phys. Rev. D* **108**, 064025 (2023), arXiv:2304.11642 [gr-qc].
- [54] S. Rosswog, P. Diener, F. Torsello, T. M. Tauris, and N. Sarin, *Mon. Not. Roy. Astron. Soc.* **530**, 2336 (2024), arXiv:2310.15920 [astro-ph.HE].
- [55] S. Chen, L. Wang, K. Hayashi, K. Kawaguchi, K. Kiuchi, and M. Shibata, arXiv:2404.18714 [astro-ph.HE] (2024).
- [56] M. R. Izquierdo, M. Bezares, S. Liebling, and C. Palenzuela, arXiv:2403.09770 [astro-ph.HE] (2024).
- [57] K. Topolski, S. D. Tootle, and L. Rezzolla, (2024), arXiv:2407.xxxxx [gr-qc].
- [58] L. J. Papenfort, S. D. Tootle, P. Grandclément, E. R. Most, and L. Rezzolla, arXiv e-prints , arXiv:2103.09911 (2021), arXiv:2103.09911 [gr-qc].
- [59] H. P. Pfeiffer and J. W. York, *Phys. Rev. D* **67**, 044022 (2003), gr-qc/0207095.
- [60] J. W. York, *Phys. Rev. Lett.* **82**, 1350 (1999).
- [61] P. Grandclément, *J. Comput. Phys.* **229**, 3334 (2010), arXiv:0909.1228 [gr-qc].
- [62] F. Foucart, L. E. Kidder, H. P. Pfeiffer, and S. A. Teukolsky, *Phys. Rev. D* **77**, 124051 (2008), arXiv:0804.3787 [gr-qc].
- [63] S. A. Teukolsky, *Astrophys. J.* **504**, 442 (1998), gr-qc/9803082.
- [64] W. Tichy, *Reports on Progress in Physics* **80**, 026901 (2017), arXiv:1610.03805 [gr-qc].
- [65] G. B. Cook and H. P. Pfeiffer, *Phys. Rev. D* **70** (2004), gr-qc/0407078.
- [66] H. Pfeiffer, *Initial Data for Black Hole Evolutions*, Ph.D. thesis, Cornell University, Ithaca, New York State (2003), gr-qc/0510016.
- [67] E.ourgoulhon, *Lecture Notes in Physics, Berlin Springer Verlag*, Lecture Notes in Physics, Berlin Springer Verlag, Vol. 846 (Springer, 2012).
- [68] A. Garat and R. H. Price, *Phys. Rev. D* **61**, 124011 (2000), gr-qc/0002013.
- [69] J. A. V. Kroon, *Phys. Rev. Lett.* **92**, 041101 (2004).
- [70] A. De Felice, F. Larroutourou, S. Mukohyama, and M. Oliosi, *Phys. Rev. D* **100**, 124044 (2019), arXiv:1908.03456 [gr-qc].
- [71] F. Foucart, M. D. Duez, L. E. Kidder, and S. A. Teukolsky, *Phys. Rev. D* **83**, 024005 (2011), arXiv:1007.4203 [astro-ph.HE].
- [72] G. Lovelace, R. Owen, H. P. Pfeiffer, and T. Chu, *Phys. Rev. D* **78**, 084017 (2008), arXiv:0805.4192 [gr-qc].
- [73] N. L. Vu *et al.*, *Phys. Rev. D* **105**, 084027 (2022), arXiv:2111.06767 [gr-qc].
- [74] N. L. Vu, arXiv (2024), arXiv:2405.06120 [gr-qc].
- [75] F. Foucart, M. D. Duez, L. E. Kidder, R. Nguyen, H. P. Pfeiffer, and M. A. Scheel, *Phys. Rev. D* **98**, 063007 (2018),



- arXiv:1806.02349 [astro-ph.HE].
- [76] S. Altıparmak, C. Ecker, and L. Rezzolla, *Astrophys. J. Lett.* **939**, L34 (2022), arXiv:2203.14974 [astro-ph.HE].
- [77] E. R. Most, L. R. Weih, L. Rezzolla, and J. Schaffner-Bielich, *Phys. Rev. Lett.* **120**, 261103 (2018), arXiv:1803.00549 [gr-qc].
- [78] M. C. Miller, F. K. Lamb, A. J. Dittmann, S. Bogdanov, Z. Arzoumanian, K. C. Gendreau, S. Guillot, A. K. Harding, W. C. G. Ho, J. M. Lattimer, R. M. Ludlam, S. Mahmoodifar, S. M. Morsink, P. S. Ray, T. E. Strohmayer, K. S. Wood, T. Enoto, R. Foster, T. Okajima, G. Prigozhin, and Y. Soong, *Astrophys. J. Lett.* **887**, L24 (2019), arXiv:1912.05705 [astro-ph.HE].
- [79] T. E. Riley, A. L. Watts, S. Bogdanov, P. S. Ray, R. M. Ludlam, S. Guillot, Z. Arzoumanian, C. L. Baker, A. V. Bilous, D. Chakrabarty, K. C. Gendreau, A. K. Harding, W. C. G. Ho, J. M. Lattimer, S. M. Morsink, and T. E. Strohmayer, *Astrophys. J. Lett.* **887**, L21 (2019), arXiv:1912.05702 [astro-ph.HE].
- [80] M. C. Miller, F. K. Lamb, A. J. Dittmann, S. Bogdanov, Z. Arzoumanian, K. C. Gendreau, S. Guillot, W. C. G. Ho, J. M. Lattimer, M. Loewenstein, S. M. Morsink, P. S. Ray, M. T. Wolff, C. L. Baker, T. Cazeau, S. Manthripragada, C. B. Markwardt, T. Okajima, S. Pollard, I. Cognard, H. T. Cromartie, E. Fonseca, L. Guillemot, M. Kerr, A. Parthasarathy, T. T. Pennucci, S. Ransom, and I. Stairs, *Astrophys. J. Lett.* **918**, L28 (2021), arXiv:2105.06979 [astro-ph.HE].
- [81] T. E. Riley, A. L. Watts, P. S. Ray, S. Bogdanov, S. Guillot, S. M. Morsink, A. V. Bilous, Z. Arzoumanian, D. Choudhury, J. S. Deneva, K. C. Gendreau, A. K. Harding, W. C. G. Ho, J. M. Lattimer, M. Loewenstein, R. M. Ludlam, C. B. Markwardt, T. Okajima, C. Prescod-Weinstein, R. A. Remillard, M. T. Wolff, E. Fonseca, H. T. Cromartie, M. Kerr, T. T. Pennucci, A. Parthasarathy, S. Ransom, I. Stairs, L. Guillemot, and I. Cognard, *Astrophys. J. Lett.* **918**, L27 (2021), arXiv:2105.06980 [astro-ph.HE].
- [82] B. P. Abbott *et al.* (LIGO Scientific, Virgo), *Phys. Rev. X* **9**, 011001 (2019), arXiv:1805.11579 [gr-qc].
- [83] C. Ecker, T. Gorda, A. Kurkela, and L. Rezzolla, arXiv e-prints, arXiv:2403.03246 (2024), arXiv:2403.03246 [astro-ph.HE].
- [84] W. Tichy, A. Rashti, T. Dietrich, R. Dudi, and B. Brügmann, *Phys. Rev. D* **100**, 124046 (2019), arXiv:1910.09690 [gr-qc].
- [85] G. B. Cook, *Phys. Rev. D* **50**, 5025 (1994).
- [86] P. Wiggins and D. Lai, *Astrophys. J.* **532**, 530 (2000), arXiv:astro-ph/9907365v2.
- [87] M. Ishii, M. Shibata, and Y. Mino, *Phys. Rev. D* **71**, 044017 (2005), arXiv:gr-qc/0501084.
- [88] M. Stockinger and M. Shibata, arXiv:2403.06834 [astro-ph.HE] (2024).
- [89] N. Straumann, *General Relativity* (2013).
- [90] J. Thornburg, P. Diener, D. Pollney, L. Rezzolla, E. Schnetter, E. Seidel, and R. Takahashi, *Class. Quantum Grav.* **24**, 3911 (2007), gr-qc/0701038.
- [91] J. Marck, Royal Society of London Proceedings Series A **385**, 431 (1983).
- [92] F. Foucart, *Front. Astron. Space Sci.* **7**, 46 (2020), arXiv:2006.10570 [astro-ph.HE].
- [93] M. Levi and J. Steinhoff, *JCAP* **01**, 011, arXiv:1506.05056 [gr-qc].
- [94] M. Levi and J. Steinhoff, *JHEP* **09**, 219, arXiv:1501.04956 [gr-qc].
- [95] M. K. Mandal, P. Mastrolia, H. O. Silva, R. Patil, and J. Steinhoff, *Journal of High Energy Physics* **2023**, 67 (2023), arXiv:2304.02030 [hep-th].
- [96] W. G. Laarakkers and E. Poisson, *Astrophys. J.* **512**, 282 (1999), arXiv:gr-qc/9709033.
- [97] G. Pappas and T. A. Apostolatos, *Phys. Rev. Lett.* **108**, 231104 (2012), arXiv:1201.6067 [gr-qc].
- [98] S. Ossokine, T. Dietrich, E. Foley, R. Katebi, and G. Lovelace, *Phys. Rev. D* **98**, 104057 (2018), arXiv:1712.06533 [gr-qc].
- [99] E. Berti, S. Iyer, and C. M. Will, *Phys. Rev. D* **77**, 024019 (2008), arXiv:0709.2589.

### Appendix A: 3+1 Reconstruction of the spacetime Riemann curvature tensor

This Appendix is dedicated to the presentation of additional details on the diagnostic quantity that can be constructed by looking at the magnitude of the Lie derivative along the helical Killing vector of the extrinsic curvature tensor, as well as to a general exposition of the necessary projections of the Riemann tensor used for computation of tidal forces. We start by recalling that the XCTS system of equations under the assumption of conformal flatness and in a 3+1 spacetime split provides the solutions for the spacetime variables  $(\psi, \alpha, \beta^i)$  and for the matter variables  $(E, p_i, S_{ij})$ . To reach our goal we need to reconstruct the Riemann curvature tensor from its projections and the right-hand side of the Einstein equations. In our notation, we will mark with a top-left index “4” the 4-dimensional spacetime tensors associated with the full spacetime metric and reserve the index 0 to denote on which position the tensor has been contracted with the normal vector to the hypersurface  $n^\mu$ .

Working in the conformally flat approximation  $\gamma_{ij} = \psi^4 \tilde{\gamma}_{ij}$ , the Ricci tensor  $\tilde{R}_{ij}$  associated with the background metric is zero and the spatial Ricci tensor can be expressed fully in terms of the derivatives of the conformal factor  $\psi$  [see, e.g., Eq. (7.42) in [67]]

$$R_{ij} = -2\tilde{D}_i\tilde{D}_j \ln \psi - 2\tilde{D}_k\tilde{D}^k \ln \psi \tilde{\gamma}_{ij} + 4\tilde{D}_i \ln \psi \tilde{D}_j \ln \psi - 4\tilde{D}_k \ln \psi \tilde{D}^k \ln \psi \tilde{\gamma}_{ij}. \quad (\text{A1})$$

Furthermore, because in 3 dimensions the Weyl tensor vanishes identically, the spatial part of the Riemann tensor (note the lack of the top-left index) is reconstructed by means of the Ricci decomposition from the spatial Ricci tensor, spatial metric, and spatial Ricci scalar  $R = R_{ij}\gamma^{ij}$

$$R_{ijkl} = -R_{il}\gamma_{jk} + R_{jl}\gamma_{ik} + R_{ik}\gamma_{jl} - R_{jk}\gamma_{il} + \frac{1}{2}R(\gamma_{ik}\gamma_{jl} - \gamma_{il}\gamma_{jk}). \quad (\text{A2})$$

The full projection onto the hypersurface can then be written using the above tensor and the extrinsic curvature  $K_{ij}$  by virtue of the “Gauss relation” [see, e.g., Eq. (3.73) in [67]]

$${}^4R_{ijkl} = R_{ijkl} + K_{ik}K_{jl} - K_{il}K_{kj}. \quad (\text{A3})$$

The projection that involves one contraction with the normal vector is given by the “Codazzi-Mainardi relation” [see, e.g., Eq. (3.81) in [67]]

$${}^4R_{i0jk} = D_k K_{ji} - D_j K_{ki}, \quad (\text{A4})$$

while the twice-normal projection usually involves the so-called Ricci equation, including the Lie derivative of the extrinsic curvature along the normal direction. Here, we will instead use an expression that requires the right-hand side of the trace-reversed Einstein equations, i.e., the contracted Gauss relation

$${}^4R_{i00j} = -R_{ij} - KK_{ij} + K^l{}_i K_{lj} - 4\pi[(S-E)\gamma_{ij} - 2S_{ij}], \quad (\text{A5})$$

where we explicitly keep the trace of the extrinsic curvature even though it is identically zero due to the maximal slicing condition that we employ for our initial data. As part of the validation of our code, we evaluated the Kretschmann curvature invariant  $\mathcal{K} := R_{\alpha\beta\gamma\delta}R^{\alpha\beta\gamma\delta}$ , which can be obtained from the expression

$$\mathcal{K} = {}^4R_{ijkl}{}^4R^{ijkl} - 4{}^4R_{i0jk}{}^4R^{i0jk} + 4{}^4R_{i00j}{}^4R^{i00j}, \quad (\text{A6})$$

where the raising of the spatial indices is performed with the spatial metric  $\gamma_{ij}$ . By evaluating the Kretschmann scalar on a number of analytical spacetimes that provide corresponding expressions in closed form (including the Schwarzschild spacetime in isotropic coordinates, as well as the de-Sitter metric), we have checked that the recovery of the full Riemann tensor from 3+1 quantities is performed correctly.

To obtain the diagnostic field  $\mathcal{L}_\xi K_{ij}$  that we have reported in Fig. 1, we make use of evolution equation for the extrinsic curvature  $K_{ij}$  in the 3 + 1 split

$$\begin{aligned} \mathcal{L}_{\partial_t} K_{ij} = & \mathcal{L}_\beta K_{ij} - D_i D_j \alpha \\ & + \alpha [R_{ij} + KK_{ij} - 2K_{ik}K_{lj}\gamma^{kl}] \\ & + 4\pi\alpha[(S-E)\gamma_{ij} - 2S_{ij}], \end{aligned} \quad (\text{A7})$$

where the evolution is carried out along some coordinate time-like four-vector  $\partial_t$ , the covariant derivative compatible with the spatial metric  $\gamma_{ij}$  is denoted by  $D_i$ , and the Lie derivative along the shift vector  $\beta$  is given by  $\mathcal{L}_\beta$ .

In the main text, we use Eq. (A7) to compute the quantity  $\mathcal{L}_\xi K_{xx}$ , which measures the deviation of the hypersurface from satisfying helical symmetry, where  $\partial_t \rightarrow \xi$  and  $\beta \rightarrow B$ . The result is monitored and reported in Table IV for various BHNS binaries, and shown in Fig. 1 for a representative case. We also note that we compute the second covariant derivative appearing in Eq. (A7) as

$$D_i D_j \alpha = \tilde{D}_i \tilde{D}_j \alpha - \tilde{\Gamma}^l{}_{ij} \tilde{D}_l \alpha, \quad (\text{A8})$$

and that the Lie derivative along the shift vector follows after using the identity

$$\mathcal{L}_\beta K_{ij} = \beta^k D_k K_{ij} + K_{ik} D_j \beta^k + K_{kj} D_i \beta^k, \quad (\text{A9})$$

where the covariant derivative can be replaced by a partial derivative because of the cancellation of the Christoffel symbols in a torsion-free spacetime.

To complete the discussion of deviations from QE and quantify the impact of BH spin and separation, in Table IV we

report volume-averaged measurements of  $\mathcal{L}_\xi \ln \psi$  and  $\mathcal{L}_\xi K_{ij}$ , calculated as follows. We define integrals over a volume  $V$

$$\|\mathcal{L}_\xi \ln \psi\| := \frac{1}{V} \int_V |\mathcal{L}_\xi \ln \psi| \sqrt{\gamma} d^3x \quad (\text{A10})$$

and

$$\|\mathcal{L}_\xi K_{ij}\| := \frac{1}{V} \int_V (\mathcal{L}_\xi K_{ij} \mathcal{L}_\xi K^{ij})^{1/2} \sqrt{\gamma} d^3x \quad (\text{A11})$$

where  $V = \int_V \sqrt{\gamma} d^3x$  is the volume of a spherical region serving as the normalization factor, and  $\gamma$  the determinant of the spatial metric  $\gamma_{ij}$ . The integrals are evaluated numerically using the Monte-Carlo method with around  $n = 6000$  points within a sphere of radius  $r = 60M_\odot$ , measured from the origin of the coordinate system. The black hole's apparent horizon is excluded from the computation domain. An inspection of the last two columns of Table IV supports the observation made already in reference to Fig. 1, namely that  $\mathcal{L}_\xi \ln \psi$  is on average an order of magnitude smaller than  $\mathcal{L}_\xi K_{ij}$ .

## Appendix B: Dependence of $E_b$ on $\chi_{\text{BH}}$

In Sec. IV C of the main text we have presented the behaviour of the binding energy as a function of the binary orbital angular frequency and we have presented in Fig. 10 a summary of the results obtained when considering BHs with different spins. We here go back to that figure and discuss the nontrivial dependence of the binding energy on the BH spin in the case of aligned spins and that, to the best of our knowledge, has not been discussed before in the literature.

More specifically, let us consider as representative examples the QE sequences with constant mass ratio shown in Fig. 10 and examine the variation of the binding energy in the case of aligned (i.e., positive) BH spins. This is reported in Fig. 14, where we show the values of binding energy at a fixed separation of  $d = 40M_\odot$  for the sequences with  $Q = 3, 5$  (black and red symbols and lines) and having total masses  $M_{\text{tot}} = 5.200M_\odot$  and  $M_{\text{tot}} = 7.800M_\odot$ , respectively (this translates to  $d/M_{\text{tot}} \approx 7.7$  and  $d/M_{\text{tot}} \approx 5.13$  in the two cases). Clearly, the binding energy does not have a monotonic behaviour with  $\chi_{\text{BH}}$ , but first decreases with spin and then increases, with a local minimum at around  $\chi_{\text{BH}} \approx 0.45$ . Note that this behaviour is present in both BHNS sequences (the sequence with  $Q = 3$  is shifted by a quantity  $-6 \times 10^{-3} M_{\text{tot}}$ , with  $M_{\text{tot}} = 5.200M_\odot$  to make it visible on the same plot; the minimum of  $E_b$  moves to around  $\chi_{\text{BH}} \approx 0.35$ ) but is not a unique feature of BHNS QE binaries. Indeed, this is shown eloquently by reporting in Fig. 14 also QE sequences of BBHs having the same mass ratio of  $Q = 5$  (purple symbols and line). Bearing in mind that BHs have zero tidal deformability and hence the corresponding binding energy at the same orbital angular velocity is (slightly) smaller, the BBH sequence exhibits essentially the same behaviour as the BHNS sequence. Of course, the fact that BBHs behave in a similar manner is helpful, but does not necessarily help explain the origin of this behaviour.

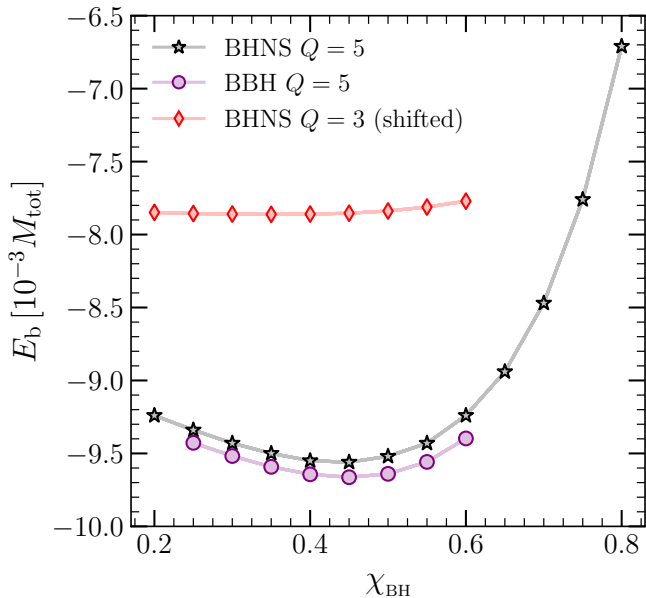


FIG. 14. Dependence of the binding energy on the BH spin for binaries at a fixed separation of  $d = 40 M_{\odot}$ . Black stars and red diamonds refer to BHNS binaries with  $Q = 5$  and  $Q = 3$ , respectively (the latter have been rescaled by a fixed amount to be shown on the same plot). Also shown with purple circles are BBH binaries with equivalent constituent masses and spins.

Hence, in order to gain a better understanding of the underlying physical grounds, we have extended the investigation presented in Fig. 14. More specifically, since the QE sequences considered refer to rather close binaries, i.e., with  $d/M_{\text{tot}} \approx 6$ , for which the assumptions behind the calculation of the initial data may be violated (e.g., conformal flatness introducing non-physical radiation content, quasi-circularity) we have explored the behaviour of  $E_b(\chi_{\text{BH}})$  also for binaries that are more widely separated, i.e., with  $d/M_{\text{tot}} \approx 12$ . In this way, we have found that the non-monotonic behaviour of  $E_b(\chi_{\text{BH}})$  is still present, although to a smaller degree, hence excluding the above-mentioned violations as the sole source of the behaviour.

Next, we have considered the contribution to the binding energy related to the spin that can be deduced from the post-Newtonian (PN) approximation. In particular, it is possible to isolate the spin-dependent contributions to the binding energy up to 3.5 PN order including cubic terms in spin [see, e.g., Eq. (5.4) of Ref. [93]] and evaluate them for spins in the range  $\chi_{\text{BH}} = 0.2 - 0.8$ , mass ratios  $Q = 3, 5$ , and for orbital frequencies  $M_{\text{tot}}\Omega \gtrsim 0.05$ . For simplicity, the expressions are all evaluated with so-called Wilson coefficients all set to unity and hence corresponding to a BBH system<sup>10</sup> [see [96, 97] in the case of a NS]. Our Fig. 14 suggests that qualitatively similar conclusions should be drawn also for a BHNS binary at these frequencies. The evaluated spin-orbit

<sup>10</sup> Wilson coefficients arise as constants in the Lagrangian of the point-particle effective action; for more details, see e.g., [94, 95].

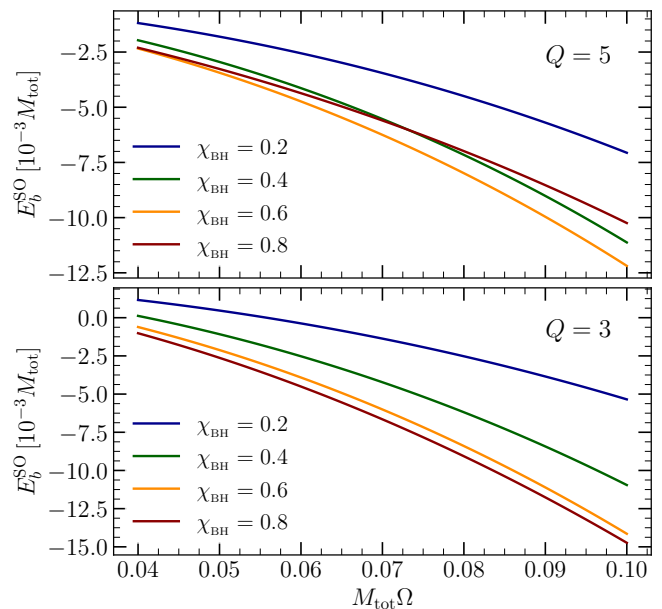


FIG. 15. Spin-orbit contribution to the binding energy of a BBH system according to Eq. (5.4) in Ref. [93] and shown as a function of the spin of the primary. The data refers to mass ratios  $Q = 5$  (top panel) and  $Q = 3$  (bottom panel).

contributions to the binding energy,  $E_b^{\text{SO}}$ , are presented in Fig. 15 and can constitute a significant part of the total binding energy if the primary is rapidly spinning. Clearly, while these contributions vary monotonically with BH spin for the mass ratio  $Q = 3$  (bottom panel), this is not the case for larger mass asymmetries of  $Q = 5$  (top panel), which is consistent with the QE picture presented in Fig. 14. Interestingly, we find that the inclusion of cubic terms in spin is essential to observe the crossing of  $\chi_{\text{BH}} = 0.2$  and  $\chi_{\text{BH}} = 0.8$  curves at  $M_{\text{tot}}\Omega \approx 0.05$  in Fig. 15, which otherwise shifts to  $M_{\text{tot}}\Omega \approx 0.075$ . Overall, while we have carried out investigations in a number of directions, the fact that the binding energy does not behave monotonically remains unclear and hence a perfect opportunity for additional studies, possibly employing dynamical simulations, as done in Ref. [98], or validation against Post-Newtonian predictions with the inclusion of spin as an extension of Ref. [99], to determine whether this behaviour is robust.

### Appendix C: Supplementary information and figures

In this Appendix we provide additional information that supplements the one illustrated in the main text. While this data is available also in the publicly released data-set, we provide it here as well for completeness. In addition, we present figures that are similar to those already presented in the main text, but refer to the different QE sequences of binaries explored in this work.

We start by reporting in Tab. IV the complete set of data relative to the binaries discussed in this paper, for a fixed mass ratio of  $Q = 5$  and with the EOS of intermediate stiffness.

These diagnostics can be readily obtained for all the QE sequences in this work by inspecting the released publicly available data.

Next, we present in Fig. 16 a representation of the  $\Omega_{\text{MS}}$  and  $\Omega_{\text{ISCO}}$  frequencies analogous to the one shown in Fig. 8, but for the soft (two left-most panels) and stiff EOSs (two right-most panels). The ADM masses of the NSs stars are fixed to the same values  $1.2, 1, 4, 1.8 M_{\odot}$ , alongside the fits with the functional forms Eq. (29) and (30) with corresponding best-fit parameters reported in Tab. II with different colours.

For the  $\Omega_{\text{MS}}$  frequencies, the impact of different compactness at the same ADM mass is clearly visible. For a given NS mass  $M_{\text{NS}}$ , the  $\Omega_{\text{MS}}$  shifts to higher frequencies for the soft EOS, indicating a later onset of mass shedding. On the other hand, the stiff EOS leads to the NS disrupting more easily than the intermediate and soft ones, and the values of  $\Omega_{\text{MS}}$  are shifted to lower frequencies accordingly. Noteworthy, for the soft EOS, the separation between the  $1.4 M_{\odot}$  and  $1.8 M_{\odot}$  se-

quences is larger than for any of the other EOSs. This is due to the largest compactness featured in this paper for the  $1.8 M_{\odot}$  NS and given by  $\mathcal{C} = 0.234$ . On the other hand, with regard to the  $\Omega_{\text{ISCO}}$  frequencies, the two EOSs feature a similar range and dependence on the mass ratio, which is comparable to the one for the intermediate EOS discussed in the main text.

Finally, Fig. 17 features a complementary picture of the QE sequences with a spinning BH, analogous to Fig. 10 in the main text, but with mass ratios  $Q = 4$  and  $Q = 6$ . While the impact of mass ratio has already been discussed at length in Sec. IV, the impact of BH spin is largely independent of the mass ratio and thus the curves at different  $\chi_{\text{BH}}$  follow the same pattern. This justifies the rescaling approach that we have chosen in Sec. IV; only a small mixed term  $\propto q \chi_{\text{BH}}$  is needed for the  $\Omega_{\text{MS}}$  frequency, whereas the rescaled  $\Omega_{\text{ISCO}}$  values for different mass ratios lie along a curve in Fig. 11 that is best described by a purely  $\chi_{\text{BH}}$  dependence.



$d$ [ $M_\odot$ ]	$d/M_{\text{tot}}$	$M_{\text{tot}}\Omega$ [ $\times 10^{-2}$ ]	$\kappa$	$E_b/M_{\text{tot}}$ [ $\times 10^{-3}$ ]	$M_{\text{ADM}}$ [ $M_\odot$ ]	$J_{\text{ADM}}$ [ $M_\odot^2$ ]	$M_{\text{K}}$ [ $M_\odot$ ]	$\delta M$ [ $\times 10^{-4}$ ]	$\ \mathcal{L}_\xi \ln \psi\ $ [ $\times 10^{-6}$ ]	$\ \mathcal{L}_\xi K_{ij}\ $ [ $\times 10^{-5}$ ]
$\chi_{\text{BH}} = -0.8$										
60.000	7.692	4.070	0.964	-2.450	7.78085	-0.772	7.78562	6.130	5.290	3.403
55.000	7.051	4.587	0.950	-2.650	7.77932	-1.032	7.78426	6.350	6.647	4.048
50.000	6.410	5.225	0.929	-2.850	7.77776	-1.206	7.78311	6.879	9.137	5.788
45.000	5.769	6.029	0.894	-2.870	7.77758	-1.196	7.78339	7.470	9.505	5.941
42.500	5.449	6.512	0.867	-2.790	7.77821	-1.097	7.78427	7.791	11.551	6.892
40.000	5.128	7.065	0.831	-2.620	7.77960	-0.905	7.78607	8.317	12.427	7.458
39.500	5.064	7.185	0.823	-2.560	7.78002	-0.853	7.78657	8.419	12.829	7.711
39.000	5.000	7.309	0.813	-2.500	7.78050	-0.794	7.78716	8.560	13.281	7.995
$\chi_{\text{BH}} = -0.4$										
60.000	7.692	4.002	0.967	-6.460	7.74959	14.595	7.75008	0.632	1.777	1.469
45.000	5.769	5.880	0.908	-7.390	7.74237	13.451	7.74323	1.111	3.606	2.645
42.500	5.449	6.338	0.887	-7.490	7.74161	13.360	7.74254	1.201	4.168	2.945
40.000	5.128	6.860	0.859	-7.510	7.74143	13.329	7.74242	1.279	4.915	3.529
39.000	5.000	7.090	0.845	-7.500	7.74148	13.336	7.74251	1.330	5.350	3.828
38.500	4.936	7.209	0.837	-7.490	7.74158	13.346	7.74262	1.343	5.599	3.977
$\chi_{\text{BH}} = 0$										
60.000	7.692	3.946	0.970	-6.940	7.74589	30.212	7.74606	0.219	0.766	0.838
55.000	7.051	4.431	0.960	-7.340	7.74278	29.586	7.74294	0.207	0.992	1.057
50.000	6.410	5.021	0.944	-7.820	7.73902	29.016	7.73926	0.310	1.314	1.358
45.000	5.769	5.758	0.919	-8.280	7.73540	28.491	7.73575	0.452	1.800	1.785
42.500	5.449	6.197	0.902	-8.510	7.73358	28.253	7.73396	0.491	2.128	2.075
40.000	5.128	6.693	0.878	-8.730	7.73194	28.042	7.73228	0.440	2.562	2.423
39.500	5.064	6.801	0.873	-8.760	7.73164	28.005	7.73197	0.427	2.664	2.502
39.000	5.000	6.911	0.867	-8.810	7.73132	27.969	7.73165	0.427	2.770	2.586
38.500	4.936	7.024	0.860	-8.840	7.73104	27.934	7.73137	0.427	2.884	2.674
38.250	4.904	7.082	0.857	-8.860	7.73092	27.919	7.73125	0.427	2.940	2.720
$\chi_{\text{BH}} = 0.4$										
60.000	7.692	3.897	0.972	-7.110	7.74456	45.909	7.74488	0.413	1.499	1.320
55.000	7.051	4.370	0.963	-7.590	7.74082	45.183	7.74114	0.413	1.767	1.401
45.000	5.769	5.655	0.928	-8.810	7.73130	43.705	7.73178	0.621	2.677	2.218
42.500	5.449	6.078	0.912	-9.150	7.72862	43.345	7.72912	0.647	3.016	2.432
40.000	5.128	6.555	0.893	-9.520	7.72577	42.990	7.72626	0.634	3.412	2.854
39.500	5.064	6.657	0.888	-9.590	7.72522	42.920	7.72570	0.621	3.496	2.923
39.000	5.000	6.763	0.883	-9.660	7.72468	42.852	7.72515	0.608	3.590	3.079
38.500	4.936	6.872	0.878	-9.730	7.72413	42.785	7.72459	0.596	3.700	3.151
38.000	4.872	6.982	0.873	-9.860	7.72313	42.706	7.72343	0.388	3.811	3.162
37.500	4.808	7.097	0.868	-9.940	7.72251	42.638	7.72280	0.376	3.926	3.235
$\chi_{\text{BH}} = 0.8$										
60.000	7.692	3.858	0.974	-3.750	7.77072	61.816	7.77496	5.456	4.874	3.041
45.000	5.769	5.572	0.933	-5.770	7.75502	59.183	7.75948	5.751	7.444	4.838
42.500	5.449	5.982	0.920	-6.210	7.75160	58.720	7.75612	5.831	7.968	5.600
40.000	5.128	6.443	0.903	-6.680	7.74786	58.248	7.75241	5.873	8.520	5.973
39.500	5.064	6.542	0.899	-6.790	7.74706	58.152	7.75161	5.873	8.779	6.099
39.000	5.000	6.644	0.895	-6.920	7.74602	58.051	7.75045	5.719	9.050	6.245
38.500	4.936	6.749	0.890	-6.980	7.74552	57.961	7.75006	5.861	9.321	6.406

TABLE IV. Most relevant quantities for the QE sequences presented in this paper and relative to the EOS with intermediate stiffness and binaries with mass ratio  $Q = 5$ , NS mass of  $M_{\text{NS}} = 1.3 M_\odot$ , total mass  $M_{\text{tot}} = 7.8 M_\odot$  (see the Data-Availability section for information on the full data-set). For each sequence with constant BH spin  $\chi_{\text{BH}}$ , we report: the initial separation  $d_0$ , the dimensionless initial separation  $d_0/M_{\text{tot}}$ , the dimensionless orbital angular velocity  $M_{\text{tot}}\Omega$ , the mass-shedding diagnostic  $\kappa$ , the dimensionless binding energy  $E_b/M_{\text{tot}}$ , the total ADM mass  $M_{\text{ADM}}$  and ADM momentum  $J_{\text{ADM}}$ , the Komar mass  $M_{\text{K}}$ , the (dimensionless) virial error  $\delta M$  [cf., Eq. (11)], as well as volume-averaged deviations from QE  $\|\mathcal{L}_\xi \ln \psi\|$  and  $\|\mathcal{L}_\xi K_{ij}\|$ .

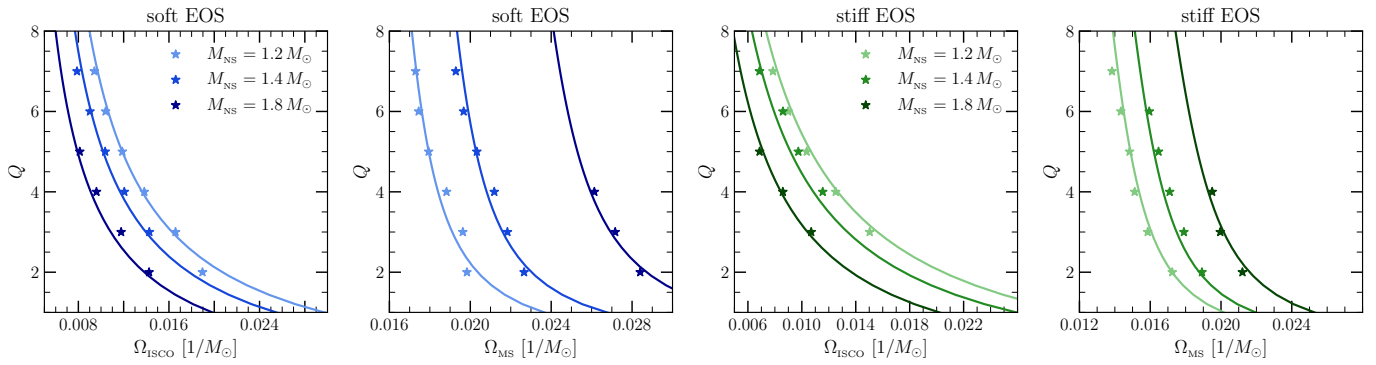


FIG. 16. (The same as Fig. 8, but for the soft EOS (leftmost panels) and for the stiff EOS (rightmost panels).

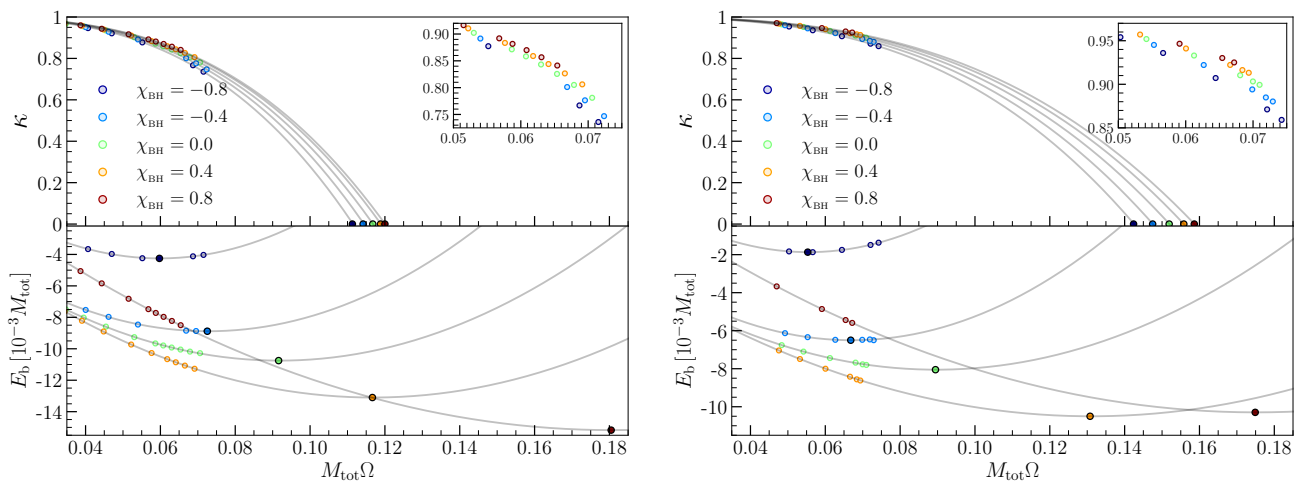


FIG. 17. The same as in Fig. 10, but for BHNS binaries having either mass ratio  $Q = 4$  (left panel) or  $Q = 6$  (right panel).